Drag of a surface piercing cylinder in fast current and low waves

A.D. Boon

On the drag of a vertical surface piercing cylinder for supercritical to transcritical Reynolds numbers and low Keulegan-Carpenter numbers

TU Delft

Thesis for the degree of MSc in Marine Technology in the specialization of ship hydromechanics

Drag of a surface piercing cylinder in fast current and low waves

By

A.D. Boon

This thesis is classified as confidential in accordance with the general conditions for projects performed by the TU Delft.

20-11-2020

Thesis exam committee

Chair/Responsible Professor:	Dr. ir. P. R. Wellens
Staff Member:	Dr. ir. G. H. Keetels
Staff Member:	Ir. M. van der Eijk

Author Details

Studentnumber:	4354265
Author contact e-mail:	adymfnaboon@gmail.com

TU Delft

Preface

The current report is based on experiments and simulations. It is written to fulfil the graduation requirements of the master program Marine Technology at the Delft University of Technology.

This project was undertaken at the suggestion of P. R. Wellens to further research at the Delft University of Technology. He thought I might find an interesting topic and he was right. I do not only find it fascinating but I also learned a lot from doing this research.

This study could not have been done without the generous support which I received. I would like to thank especially J. G. den Ouden, C. P. Poot, J. Rodrigues Monteiro, and P. Chabot for designing and helping to carry out the experiments. Thank you for keeping an open mind towards this research, which tested the limits of the towing tank. Your attentiveness and ingenuity have led to a successful conclusion. Thank you to P. R. Wellens for the patience and guidance and your gentle nudges in the right direction when needed. Of course, without you, none of this would have happened. Special thanks to M. J. Kleijwegt for providing the computational and storage capacity for the simulations and research data. Last but not least, thank you to all those with whom I discussed this study and my approach and who provided valuable feedback by challenging my ideas.

And then finally, to you, the reader: I hope you will enjoy reading about this study and its conclusions.

A.D. Boon
Delft, October 2020

Summary

With the transition towards renewable energy, offshore wind power farms are being constructed or planned in many places involving placing wind turbines in the sea. The monopiles for these wind turbines are vertical cylinders which are situated in a flow with high Reynolds numbers and low to intermediate Keulegan-Carpenter numbers. The Reynolds and Keulegan-Carpenter number are dimensionless numbers for the quantification of respectively currents and waves.

Previous research has not covered the Reynolds and Keulegan-Carpenter numbers in which energy generating devices are situated. The current research is focused on filling the gap and investigating the drag forces on these cylinders via means of experiments. Additional simulations focussing on the free surface and end effects were also conducted. The forces at play and the Morison equation to model these forces have been evaluated.

It was discovered that in the investigated range, the drag and inertia coefficients depend on both Reynolds and Keulegan-Carpenter numbers. By analyzing the results of the experiments in the time and frequency domain, indications of vortex shedding and second-order harmonic wave forces, as well as forces from wave-wave interaction were found. The Morison equation itself is analyzed to find that it either underestimates or neglects these forces. By means of simulations, the effects of the free surface and the aspect ratio of the cylinder on the drag and inertia coefficients are found. Lastly, it is proposed to use a rewritten Morison equation to find the drag on a cylinder in a flow with irregular waves. This equation is found to describe the drag forces more accurately.

Contents

Nomenclature

C_D	Drag coefficient [-]
F_D	Drag force [N]
ρ	Water density [kg/m^3]
U	Relative velocity [m/s]
D	Diameter cylinder [m]
C_M	Inertia coefficient [-]
F_I	Inertia force [N]
$\dot{U}$	Relative acceleration [m/s^2]
Re	Reynolds number [-]
U_c	Relative current velocity [m/s]
ν	Kinematic viscosity water [m^2/s]
KC	Keulegan-Carpenter number [-]
U_m	Relative oscillatory water particle velocity [m/s]
T	Wave period [s]
F	Force [N]
L	Underwater length cylinder [m]
β	Frequency number [-]
St	Strouhal number [-]
f_w	Vortex shedding frequency [Hz]
V_r	Reduced velocity parameter [-]
f_n	Natural frequency [Hz]
L_T	Total length cylinder [m]
H_s	Significant wave height [m]
T_{av}	Average wave period [s]
U_{av}	Average current velocity [m/s]
σ_U	Deviation in velocity [m/s]
T_p	Peak wave period [s]
H_w	Wave height regular waves [m]
λ	Wave length [m]
H_{bi}	Wave height bichromatic waves [m]
γ	Peak enhancement factor [-]
LS	Least Squares
LSFD	Least Squares Frequency Domain
R	Residual [N^2]
F_{meas}	Measured drag force [N]
F_{comp}	Computed drag force [N]
T_m	Measured time [s]
t	Time [s]
f_{max}	Highest measurable frequency [Hz]
f	Frequency [Hz]
t_0	Start time of individual wave [s]
μ_c	Mean value coefficient [-]
σ_{unc}	Variance due to uncertainty [-]
σ_{data}	Variance found in data [-]
RMS_t	Root mean squared of the residual in the time domain [N]
RMS_f	Root mean squared of the residual in the frequency domain [N]
VOF	Volume of Fluid
V	Control volume [m^3]
$\boldsymbol{u}$	Velocity vector [m/s]
$\boldsymbol{n}$	Normal at boundary [-]
p	Pressure [N/m^2]
∇	Gradient operator [-]
$\boldsymbol{F}$	External body force vector [N]
Fr	Froude number [-]
g	Gravitational acceleration [m/s^2]
R^2	Coefficient of determination [%]
ω	Angular frequency [rad/s]
ϵ	Phase shift [rad]
B	Width tank [m]
n_w	Number of wheels on carriage [-]
m	Mass of carriage [kg]
$F_{M_{max}}$	Estimated maximum drag force [N]
F_g	Gravitational force [N]
F_w	Force on wheel [N]
c_f	Friction coefficient [-]
a_a	Acceleration [m/s^2]
a_d	Deceleration [m/s^2]
L_{tank}	Driving length tank [m]
t_{stab}	Estimated stabilizing time [s]
$t_{test_{min}}$	Minimum test time [s]
η_{meas}	Measured average wave height [m]
η_{lin}	Linear wave amplitude [m]
η_{max}	Maximum measured wave height [m]
H_{m0}	Spectral significant wave height [m]

1 Introduction

A global effort is put into transitioning towards renewable energy. This effort has pushed energy generating devices out into the sea, to harvest the energy from waves, winds and the sun. Energy generating devices are commonly in the shape of vertical cylinders, like monopiles, wave energy converters, or parts of offshore solar fields [3, 11, 26, 59]. Currents and waves induce hydrodynamic forces as structures are placed in them. Much of the area at sea can not yet be exploited with the current knowledge as methods used now to estimate the forces lead to incorrect estimations [44, 46]. Improving the estimate of the drag of these cylinders will allow for less conservative design, leading to an improved economic incentive to build energy generating devices for renewable energy.

1.1. Background

A cylinder is a simple geometry, but in a flow, it creates complex phenomena.

To be able to predict forces on cylinders in flow, the drag coefficient, C_D, and the inertia coefficient, C_M, are used. They are shown in equation 1.1. C_D is used to find the drag forces and C_M is used to find the inertia forces. In this equation F_D denotes the drag force, ρ the water density, U the relative velocity between the water and cylinder, D the diameter of the cylinder, F_I the inertia force and $\dot{U}$ the relative acceleration.

$$C_D = \frac{F_D}{0.5\rho U^2 D} \qquad C_M = \frac{F_I}{0.25\pi\rho\dot{U}D^2} \tag{1.1}$$

1.1.1. Reynolds (1883)

O. Reynolds studied laminar and viscous flows and the transition between them. His research introduced the Reynolds number (Re). The quantification of the regime of the flow creates the ability to predict the boundary layer, turbulence and possible turbulence patterns around an object, which then again lead to predictions of C_D [77]. Equation 1.2 shows the formulation of Re, in which ν is the kinematic viscosity of water and U_c the relative current velocity.

$$Re = \frac{U_c \cdot D}{\nu} \tag{1.2}$$

In research, it has been stated that the drag coefficient depends on only the Reynolds number, the surface roughness and the geometry [19]. However, when research continued, it was found that the drag coefficient also depends on oscillations in the flow.

1.1.2. Morison (1950)

The Morison equation is a semi-empirical equation developed by J.R. Morison, J. Johnson, and S. Schaaf on the forces on a cylinder in oscillatory flow [71]. The theory was developed using experimental results and the equations of velocity and acceleration of water particles due to waves of small amplitude. The equation resulting from the research separates two out of phase force components: 1) a drag force proportional to the square of the velocity and 2) an inertia force proportional to the horizontal component of the acceleration [57]. The Morison equation, shown in equation 1.3, requires a known drag coefficient and inertia coefficient,

often obtained from approximations or empirically [44]. In equation 1.3, L is the underwater length of the cylinder.

$$F = \underbrace{\frac{1}{2} \cdot \rho \cdot D \cdot L \cdot C_D \cdot U|U|}_{1} + \underbrace{\frac{1}{4} \cdot \pi \cdot \rho \cdot D^2 \cdot L \cdot C_M \cdot \dot{U}}_{2} \tag{1.3}$$

A modification on the Morison equation has also been used. This modification separates the drag force into a static and oscillatory part, leading to three terms in the Morison equation [86]. This is done to separate steady and oscillatory fluid motion [48] or to separate the flow and the periodic movement of the cylinder [56]. The three-term Morison equation is further discussed in paragraph 4.5.

1.1.3. Keulegan-Carpenter (1958)

Up to 1958, the oscillatory properties of the flow compared to the structure were not cohesively described. G. H. Keulegan and L. H. Carpenter found a way to describe this while investigating the inertia and drag coefficients of cylinders and plates in sinusoidal currents [47]. The Keulegan-Carpenter number in equation 1.4 was introduced. In this equation U_m is the relative water particle velocity and T is the wave period.

$$KC = \frac{U_m \cdot T}{D} \tag{1.4}$$

The numerator is proportional to the stroke of the motion. This means that if the KC number is small, the orbital motion of the water particles is small, indicating low waves relative to the cylinder. This number can predict, similar to the Reynolds number, flow patterns [8]. As Morison, Johnson, and Schaaf had previously found, Keulegan and Carpenter also concluded that the drag coefficient indeed does not only depend on the Reynolds number, but also the Keulegan-Carpenter number.

1.1.4. From 1960 onwards

The Morison equation can be used to find the forces on a cylinder in waves and currents. However, what values of C_D and C_M should be used, how these values can be found and the flow effects that occur and their influence is still a topic of research. Venugopal et al. [85], Sumer [77] and Sarpkaya [70] are some that research the hydrodynamic forces on the cylinder. Bearman [6], Rockwell [66], Thorson [80] and Zdravkovich [93] are more focused on the wakefield and simulating it. The work of Sarpkaya and Bearman is discussed as their contributions give insight into the problem.

T. Sarpkaya

Sarpkaya [67] created an overview of C_D and C_M with experiments for $100 < \text{Re} < 1.44 \cdot 10^6$ and $0.17 < \text{KC} < 80$. With this research he found a dependency of C_D and C_M on the frequency number, β (equation 1.5). β is still used to evaluate C_D and C_M. It is inversely proportional to the Stokes number. A connection between the Stokes number and the flow around cylinders was previously found. Now it is known that it is a representation of the relationship between Re and KC [70].

$$\beta = \frac{Re}{KC} \tag{1.5}$$

P.W. Bearman

Bearman mostly focused on the flow behind cylinders in higher ranges of the Re and KC. Bearman's research continued on previous work. In this previous work, a coefficient for vortex shedding was found, the Strouhal number (St) shown in equation 1.6, in which f_w is the vortex shedding frequency. This is the vortex shedding frequency in the flow around a fixed cylinder at a fixed Reynolds number [6].

$$St = \frac{f_w D}{U} \tag{1.6}$$

Bearman's work includes experiments and simulations looking into vortex shedding and vortex-induced vibrations (VIV). VIV is important for the fluid-structure interaction (FSI) of cylinders on springs as fluid-induced motion (FIM) is excited. This motion drastically influences the drag (and lift) forces on the cylinder [8]. Previous work had found that vortex shedding can lead to resonant synchronization, influencing the forces. It is correlated to the reduced velocity parameter (V_r) [90], shown in equation 1.7. In this equation, f_n is the natural frequency in a vacuum.

$$V_r = \frac{U}{f_n D} \tag{1.7}$$

1.1.5. Simulations

Work has started on simulating this problem, as computational power is now available to researchers. Modelling of a cylinder in high Reynolds numbers is known to be problematic [73]. Tools which use empirical and semi-empirical solutions relying on hydrodynamic force coefficients found in experiments are developed, such as SHEAR7, VIVA, and VIVANA. However, these methods are still subject to large uncertainties. So large even, that safety factors of 10 to 20 are required [87].

Modelling the problem for high Reynolds numbers using computational fluid dynamics (CFD) is an active field of research. Extensive research into the modelling methods at the critical regime of Reynolds numbers using the turbulence models Reynolds Averaged Navier-Stokes (RANS), Detached Eddy Simulations (DES) and Large Eddy Simulations (LES) was conducted by Qiu et al. [63]. After this research from 2017, new research was conducted by Sreenivasan and Iyer [73] and [2] on (wall) turbulence models for high Reynolds numbers between $2{\cdot}10^4$ and $1{\cdot}10^6$, and CFD predicted C_D by Xiang and Guedes Soares [91]. This research brings promising results, but despite the extensive work done, modelling of turbulent flow over cylinders at high Reynolds numbers continues to be a challenge [73].

1.1.6. Overview of research

With the help of overviews created by Sumer and Fredsoe [76] and Sreenivasan [73] the ranges which have been previously researched are shown in table 1.1. In this table, it can be found that no research has been done for high Reynolds numbers ($Re > 1.4{\cdot}10^6$) and low to intermediate Keulegan-Carpenter numbers ($0.17 < KC < 3$), as was also stated by Cobbin et al. [20] and Sumer and Fredsoe [76]. This is problematic as these are the ranges in which energy generators are situated, as paragraph 1.2 shows.

Table 1.1: Researched values of Re and KC numbers. The asterisk show that the research investigated irregular waves. Note that for Morison et al. no values for KC are known as Keulegan and Carpenter's research had not yet been published. Dean et al. [22] used measured forces on a monopile, without a known wave spectrum, and thus reported no KC values either

Current and oscillatory flow

	Reynolds		Keulegan-Carpenter	
	min	max	min	max
Verley and Moe [86]	$5{\cdot}10^2$	$2.5{\cdot}10^4$	3.8	6.1
Sarpkaya [69]	$1.75{\cdot}10^2$	$1.44{\cdot}10^6$	0.17	1
Sarpkaya [68]	$1{\cdot}10^2$	$6{\cdot}10^3$	0.5	3.2
Honji [76]	$5{\cdot}10^2$	$5{\cdot}10^3$	1.2	2.2
Williamson [89]	$1{\cdot}10^3$	$7{\cdot}10^3$	4	35
Justesen [45]	$1{\cdot}10^3$	$2{\cdot}10^5$	7	15
Aristodemo et al. [5]	$1.74{\cdot}10^4$	$3.64{\cdot}10^4$	4.4	8
Høgedal et al. [76] *	$1{\cdot}10^4$	$5{\cdot}10^4$	2	35
Shankar et al. [72]*	$3{\cdot}10^3$	$3.8{\cdot}10^4$	0.5	28

End effects, current and oscillatory flow

	Reynolds		Keulegan-Carpenter	
	min	max	min	max
Moe et al. [56]*	$2.9{\cdot}10^5$	$1.2{\cdot}10^6$	7.6	37
Boccotti et al. [9]*	$2.5{\cdot}10^4$	$2{\cdot}10^5$	4	30
Bearman et al. [7]	$1.5{\cdot}10^4$	$5{\cdot}10^5$	1	20
Stansby et al. [74]*	$4{\cdot}10^3$	$1.9{\cdot}10^4$	5	25

End effects, vertical surface piercing cylinder, current and oscillatory flow

	Reynolds		Keulegan-Carpenter	
	min	max	min	max
Dean et al. [22]*	$6{\cdot}10^6$	$8{\cdot}10^7$	?	?
Morison et al. [57]	$2.2{\cdot}10^3$	$1.1{\cdot}10^4$	?	?

1.1.7. Critical reflection on existing research

During the years of research, different attempts have been made to create a method to correctly estimate the forces on a cylinder in current and waves. The discussed Morison equation is commonly used but has received critiques over the years. Morison's equation has proven effective in research [56]. However, the methodology of these researches has often been: do experiments, find C_D and C_M from them, and then check, with these coefficients, if the force from Morison's equation agrees with the force found in experiments. Most methods of finding C_D and C_M are based on the Morison equation, thus the coefficients have been calibrated to the experiment and Morison equation, thus giving good results. In practice C_D and C_M are not known [55]. Capannelli and Gudmestad [15] stated that the C_D used for North Sea Design Practice was too low and has lead to under-estimation of design loads and unsafe structures. They proposed using a new C_D, 50% higher than the value previously used, showing the inaccuracy of prediction methods.

These problems have led to the interest of researchers. Some, like Sarpkaya [70], Iwagaki and Asano [42], Yuan and Huang [92], Verley and Moe [86] and Lighthill [21] have made proposals to improve on the used methods. Lighthill proposed a correction on Morison's equation. However, as Moe and Gudmestad [56] wrote, no attempts to replace or improve Morison's equation has been successful [21]. Sarpkaya has proposed β and m, Yuan and Huang $V_R + KC_H$, Iwagaki and Asano KC_2^*, and Verley and Moe VM, all dimensionless numbers that correlate with C_D, so a correlation may be found and better estimations of these coefficients can be made in the future. However, a cohesive correlation for C_D and C_M and the many flow parameters has yet to be found [44, 56]. To find one will be challenging, as the coefficients attempt to capture multiple hydrodynamic phenomena, each acting with its own amplitude, frequency and phase. Predicting the combination and interactions and capturing it within those two coefficients is challenging.

1.2. Problem statement

The situation found in practice is investigated to find the applicability of research done.

1.2.1. Energy generators

The average dimensions of the cylinder-shaped energy generators are obtained from literature [11, 14, 52, 59]. To find the average dimensions of wind turbines, 2653 wind turbines from 30 offshore wind farms are used [59]. In practice, these monopiles have a minimum length of 21 meters and a maximum length of 85 meters. The diameter of the monopiles varied between 2.1 and 7 meters.

As wave energy converters are less common, three different designs and their dimensions are used to find the average size. The lengths of the designs vary between 23 and 44.3 meters, and the diameter between 0.3 and 9.5 meters [11, 52]. The averages are shown in table 1.2. In this table L_T is the total length.

Designs for a new kind of offshore energy generating device is also emerging: offshore solar fields. Some initial designs for these consist of structures made up of buoys, shaped as vertical, surface piercing cylinders [3, 26]. These designs are in such an early stage of development, that no dimensions are known.

Table 1.2: Average dimensions of vertical cylindrical energy generators

	L_T [m]	D [m]
Monopile windturbine	51	4.8
Wave energy converter	33	4.2

1.2.2. Environmental conditions

Not only the dimensions of the design are of importance, but also the location is. This determines the flow in which the device is situated. For different parts of the world, area's where these kind of devices might be placed are looked into [13, 18, 51, 52, 54, 62, 78]. The average over a larger area and over time is shown in table 1.3. In this table H_s is the significant wave height, T_{av} the average wave period and U_{av} the average current velocity.

Table 1.3: Average parameters for various area's at sea where energy generators might be placed

	Depth [m]	$H_{s_{min}}$ [m]	$H_{s_{max}}$ [m]	$T_{av_{min}}$ [s]	$T_{av_{max}}$ [s]	U_{av} [m/s]	Re [-]	KC [-]
North Sea	51	1.3	2.7	5	7	0.38	$1.4{\cdot}10^6$	0.9
South China Sea	33	0.9	3.2	5.5	7	1.6	$5.8{\cdot}10^6$	1
U.S. Coast	75	0.6	1.6	5.7	7.9	0.35	$1.3{\cdot}10^6$	0.5

The values shown are the main parameters of wave spectra. A wave spectrum is a representation of a real sea state which is irregular and unsteady. An ocean wave spectrum will vary over time and location. Models have been created to capture the average sea state for certain area's. A well known and often used spectrum is the JONSWAP spectrum, developed for the North Sea [35]. For design purposes, the JONSWAP spectrum is applicable for many areas, such as around South-America, Australia and Africa [16]. For other area's like the South China Sea, research is done to find an applicable wave spectrum model [53].

For Re and KC alternative formula's for irregular oscillatory flow are established, shown in equation 1.8 [50]. In these equations σ_U is the deviation in velocity and T_p the peak wave period.

$$Re = \frac{\sqrt{2}\sigma_U \cdot D}{\nu} \qquad KC = \frac{\sqrt{2}\sigma_U \cdot T_p}{D} \tag{1.8}$$

1.3. Objective

From the research into the energy generators and their environment, it is found that energy generators are situated in flow with high Reynolds numbers and low to intermediate Keulegan-Carpenter numbers in irregular waves as shown in table 1.4. The energy generators pierce the surface and they can have a free end, inducing free surface effects at the water-air interface and end effects. It is known that it is not possible to reliably estimate the forces for this situation [15, 55]. The ranges in table 1.1 covered by previous research show that the situation in practice is not covered by existing research, as was also found by previous researchers [9, 44]. The gap for Re and KC is visualized in figure 1.1. The efforts in this thesis are focused on finding C_D and C_M and to investigate the drag forces on a cylinder in high Reynolds and low Keulegan-Carpenter numbers using experiments.

Table 1.4: Showing the discrepancy of the ranges of Re and KC previously researched and found in practice, and showing the scope of the current research

	Re	**KC**
In practice	$1.2{\cdot}10^6$ - $6.3{\cdot}10^6$	0.2 - 3.1
Previously researched	$1{\cdot}10^3$ - $1.4{\cdot}10^6$	0.17 - 80
Current research	$9.7{\cdot}10^5$ - $2.0{\cdot}10^6$	0.49 - 1.9

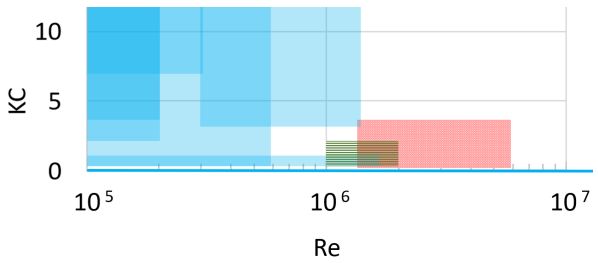

Figure 1.1: Visualized gap in existing research. Researched values from table 1.1 in solid blue, the situation in practice in dotted red and scope of the current researched in green vertical lines. Note that there is little overlap between the previous research and the values found in practice

1.3.1. Goal

Investigating the variations of the drag of a vertical surface piercing cylinder in waves and current at high Reynolds numbers and low Keulegan-Carpenter numbers

Research questions

1. *Is the drag coefficient mainly dependent on the frequency of the incoming waves?*
2. *How can the drag of a cylinder in irregular waves and current be modelled?*
3. *Do the forces on a cylinder correlate to any of the non-stochastic parameters of the flow?*

1.3.2. Modelling the problem

To fulfil the stated goal experiments are conducted. The effects of current velocities are important to find the dependency of the wave frequency on the drag, thus the current velocity has been varied as well as the wave frequency [32]. The effects of the waves, the free surface effects and end effects depend on the dimensions of the cylinder [12, 65, 66]. To minimize interference of surface roughness, hydroelasticity, piston-mode, or wall effects, the cylinder will be a smooth, rigid and solid cylinder with a constant diameter in a water-filled basin with dimensions following the ITTC guidelines [41]. The free end of the cylinder and the free surface are of interest and thus included in the research. The experiments were scaled for Re and KC. This means that the surface effects, which scale differently, will not be realistic. The effect this and the end effects have on the results is investigated in paragraph 3. The flow is uniform, unidirectional, with constant current and unidirectional waves in the same direction. Regular, bichromatic and irregular waves are tested, as there is a gap in research for all wave types. For irregular waves, the JONSWAP model is used, as it is one of the three models recommended by the ITTC [40]. The values tested are shown in table 1.5. The choice for them is explained in paragraph A.1 in the appendix.

Table 1.5: Re and KC numbers considered in the current research

Re	$9.71{\cdot}10^5$	$1.08{\cdot}10^6$	$1.19{\cdot}10^6$	$1.30{\cdot}10^6$	$1.41{\cdot}10^6$	$1.52{\cdot}10^6$	$1.89{\cdot}10^6$	$2.02{\cdot}10^6$
KC	0.49	0.75	1.1	1.5	1.9			

2

Experiments

To research the problem it was chosen to conduct experiments. A detailed description of the choice of methodology, facility, and the designing of the experiments is given in appendix A. In this chapter, the experiments are summarized and the data processing method is discussed.

2.1. Experimental setup

The setup adheres to the modelling of the problem as described in paragraph 1.3.2. As such, it is a stiff, smooth, closed cylinder with a constant diameter. Due to the large forces expected on the model, the design choice was made to use a primary lever setup. A cross-section of the test setup is shown in figure 2.1. In the setup, the drag force and the distance of the pivot point to the application point of the drag force are the quantities of interest. These are found using loadcells placed such that the forces in the x-direction are measured. The positive x-direction is defined in the direction of current and waves. The design process of the experiments and discussion on the experimental setup is shown in appendix A.

Figure 2.1: Left: photograph of the test setup, model shown in yellow. Right: 2D model of the test setup, distances are given in millimetres

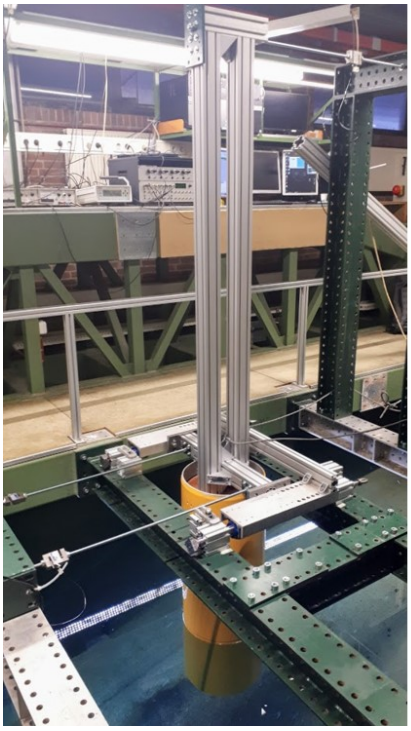

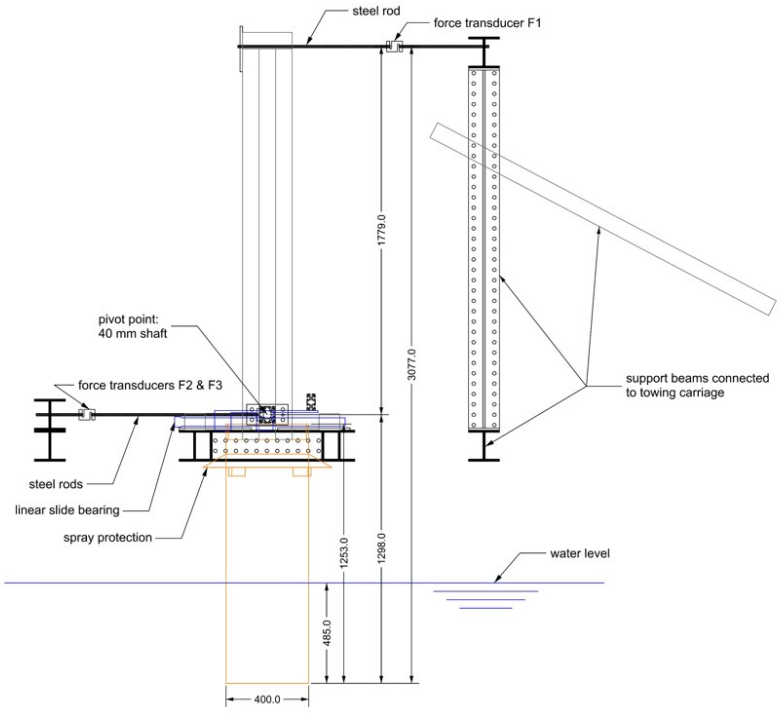

The setup was build using steel H-beams of 0.15 x 0.15 m cross-section, creating a stiff structure. Aluminium beams of 0.08 x 0.08 m cross-section were used to further stiffen the setup. Three loadcells of the type H3-C3-200kg-3B by Zemic were used. A PVC pipe was used as the cylinder. Spray protection, not shown in the photograph in figure 2.1, was placed on the top of the cylinder to protect the electronics. The roundness of the cylinder was checked and a maximum difference in diameter of 0.3% was found. The measurements can be found in appendix A. The cylinder was treated until a smooth surface was achieved.

2.2. Test plan

The velocity, wave period, wave height and wave type are varied. As the ranges of KC are well researched, the choice was made to have a larger range of Reynolds numbers. Thus for the current velocity and wave period, respectively eight and five different data points are tested. All tests are repeated between two to four times to evaluate the consistency of the results. The values that are tested are chosen to achieve the goal of the research while being within the limits of the test facility, as discussed in appendix A. The values are shown in table 2.1. In this table T_p is the peak wave period of a wave spectrum.

Table 2.1: Values of U, T, T_p and wave types tested and the resulting Re and KC values

U [m/s]	3.00	3.34	3.68	4.02	4.36	4.70	5.04	5.38
T or T_p [s]	1.0	1.24	1.48	1.72	1.96			
Wave type	Harmonic	Bichromatic	Regular					
Re	$9.7{\cdot}10^5$	$1.1{\cdot}10^6$	$1.2{\cdot}10^6$	$1.3{\cdot}10^6$	$1.4{\cdot}10^6$	$1.5{\cdot}10^6$	$1.9{\cdot}10^6$	$2.0{\cdot}10^6$
KC	0.49	0.75	1.1	1.5	1.9			

2.2.1. Wave modelling

The research investigates regular, bichromatic and irregular waves for the reasons discussed in paragraph 1.3.2. The waves are created using a flap-type wavemaker in the towing tank. The wave parameters are shown in table 2.2. In this table H_w is the wave height of regular waves, λ the wavelength, H_s the significant wave height of a wave spectrum, and H_{bi} the wave height of bichromatic waves.

The regular waves are modelled with a constant H_w/λ of 1/25. This allows for stable waves during experiments and larger values of KC, as opposed to using less steep waves. The irregular waves are modelled according to the JONSWAP spectrum as described in the literature and the ITTC guidelines [33, 40, 61]. The JONSWAP spectrum is modelled to be dependent on T_p and the peak enhancement factor (γ). Spectra are created with T_p equal to the regular wave period tested, γ is kept constant at the typical value of 3.3, which resembles an intermediate wind-wave growth state.

Table 2.2: Parameters of the waves used during tests. The bichromatic waves are a combination of T = 1.24 & 1.72 s, and T = 1.24 & 1.96 s

T or T_p	1.0 s	1.24 s	1.48 s	1.72 s	1.96 s
H_w	0.055 m	0.094 m	0.14 m	0.19 m	0.24 m
λ	1.6 m	2.4 m	3.4 m	4.6 m	6.0 m
H_s	0.06 m	0.1 m	0.14 m	0.18 m	0.24 m
H_{bi}		0.05 m		0.09 m	0.12 m

2.3. Data processing

For this research C_D and C_M have to be obtained from the force data as these give insight into the forces and their dependency on KC and Re. There are many methods to find C_D and C_M, such as method of moments, Fourier series approach, Fourier average approach, weighted least squares, least squares (LS) method and least-squares frequency domain (LSFD) method [39, 64]. Each method will yield different values for C_D and C_M, as none of these methods can determine exact values for C_D and C_M [44]. However, literature shows that the LSFD method is the most reliable [64]. Still, because of the variance between methods, both the LS method and LSFD method are chosen to determine the coefficients to compare. These can both be used for irregular waves and both use the entire time record which will give more accurate results.

Least Squares method (LS)

The LS method uses equation 2.1, with which C_D and C_M can be determined. By minimizing the residual, coefficients are found. In this equation F_{meas} is the measured drag force in the time domain, F_{comp} the computed drag force and T_m the measured time and t indicates time.

$$R = \int_0^{T_m} (F(t)_{meas} - F(t)_{comp})^2 dt \tag{2.1}$$

The LS method is stated to be reliable and accurate [39], and it can be applied to irregular waves [85]. However, with this method, small phase shifts can lead to large inaccuracies in the estimated coefficients. Also, as shown in equation 1.3, particle velocity and acceleration for the irregular wave field need to be known. This is found using the method described by Donelan et al. [24] in his second chapter. This method is only valid within a certain time window due to the limited time observation of the spectrum [58]. It should be noted that this method uses the dispersion relation and thus assumes the waves to be fully linear, which they are not completely. This, combined with measuring errors, can lead to a phase shift between the estimated and actual velocity and acceleration of the particles. This, in turn, will lead to inaccurate results when using this method.

Least Squares Frequency Domain method (LSFD)

The LS method can also be performed in the frequency domain. This can be computed using equation 2.2. In this equation f indicates frequency and f_{max} the highest measurable frequency, for these experiments that is 100 Hz.

$$R = \int_0^{f_{max}} (F(f)_{meas} - F(f)_{comp})^2 df \tag{2.2}$$

As the residuals are calculated in the frequency domain, more importance is given to accurately representing the frequency of the force.

A problem with the LS methods is that a small phase shift can cause inaccurate results [64]. That does not occur when applying the LSFD method.

2.4. Error analysis

The results from the experiments after data processing have been evaluated using error analysis.

First, the error that occurs due to known measuring deviations is estimated and an uncertainty interval (σ_{unc}) is identified. To find this uncertainty, the data processing steps were repeated with the uncertain variables changed to include the perceived level of inaccuracy, discussed in appendix A. For each run, the maximum variance of the values was used, and then the average of the variance for all the runs was obtained. The results are shown in table 2.3, showing the mean value μ_c as well. A large difference in μ_c for C_M is found, as the LS method estimates C_M to be zero if there are phase shifts between the measured and computed forces.

Secondly, the spread of data is calculated, using the variance of all the tests that were repeated. The average of all the runs was used. Tests were repeated two to four times. The overall average variance is used. The variance of the spread of data (σ_{data}) can be found in table 2.3.

The root mean squared (RMS_t) of the residual from equation 2.1 should show the accuracy of the estimated coefficients. However, first, note that noise and phase shifts will increase the RMS_t values. The RMS_t method will thus favour the LS method as it compensates for a phase shift by tuning the coefficients. This is why this method is also implemented for the frequency domain by using the root mean squared of the residual from equation 2.2 (RMS_f). RMS_t and RMS_f were normalized to compared to literature using formula 2.3. The normalized values in previous research are in the range of 0 to 0.05 for KC < 2 [48]. The results in table 2.3 show that in the frequency domain the results are as accurate, but in the time domain they are not.

$$\Delta F_{\text{RMS}} = \frac{2 \cdot RMS}{\max(F_{meas}) - \min(F_{meas})} \tag{2.3}$$

Table 2.3 shows the results of the error analysis. The spread in the data is slightly larger than the expected spread in data due to uncertainty. However, the difference for the LSFD method is limited and thus deemed acceptable.

The error analysis showed that the LSFD method gives more consistent results for the coefficients, which is in line with literature [64]. This method is thus used. For the additional experiments without waves, this method is not applicable so the LS method is used.

Table 2.3: Error analysis for both the LS and LSFD method, shown are the averages for all experiments

		μ_c	σ_{unc}	σ_{data}	RMS_t	RMS_f	ΔF_{RMS_t}	ΔF_{RMS_f}
LS	C_D	0.45	0.0034	0.0045	150	8.1	0.30	0.024
	C_M	1.01	0.26	0.30				
LSFD	C_D	0.46	0.0024	0.0048	167	7.5	0.31	0.023
	C_M	2.47	0.15	0.14				

3

Simulations

As stated in paragraph 1.1.5, research is currently focused on improving simulation methods for the problem at hand. A need for simulations is there as scaling combined with a focus on the Reynolds numbers in the experimental research leads to the experiments mostly being conducted at high Froude number, larger then is expected for true scale energy generating devices. Also, end effects dependent on the length over diameter ratio influence on C_D, making it difficult to apply experimental results to realistic cases with different geometries. Using simulations these aspects are further investigated. The objective is to evaluate the free surface effects and end effects on a vertical surface piercing cylinder, using simulation methods to examine experimental results. Simulations should include viscosity to simulate the Reynolds dependent effects. ComFLOW is used as it is specifically designed for viscid flow simulations including free surface.

In this chapter, ComFLOW and the setup of the simulations are discussed. In paragraph 4.4 the results from the simulations are shown.

3.1. ComFLOW

ComFLOW is a numerical method for the simulation of fluid flow with a free surface, based on the Navier-Stokes equations [83]. It employs a finite volume discretization. The Volume of Fluid (VOF) method is used to displace the free surface. It can deal with run-up, wave breaking and water-on-deck situations [36].

Governing equations

The one-phase flow model is used. It assumes that the effect of air can be neglected and models it as a vacuum. Conservation of mass is described by the continuity equation and conservation of momentum by the Navier-Stokes equation. The conservative form of the equations are shown respectively in equation 3.1 and 3.2. The incompressible form of the equations are used as water is modelled as an incompressible viscous liquid, which is realistic for the expected conditions. In these equations ∂V is the boundary of the control volume V, $\boldsymbol{u}$ is the velocity vector in the x, y and z directions: (u, v, w), the normal at the boundary is indicated with $\boldsymbol{n}$, p is the pressure, ∇ the gradient operator and $\boldsymbol{F} = \left(F_x, F_y, F_z\right)$ the external body force [79].

$$\oint_{\partial V} \boldsymbol{u} \cdot \boldsymbol{n} dS = 0 \tag{3.1}$$

$$\int_V \frac{\partial \boldsymbol{u}}{\partial t} dV + \oint_{\partial V} \boldsymbol{u}\boldsymbol{u}^{\mathrm{T}} \cdot \boldsymbol{n} dS = -\frac{1}{\rho} \oint_{\partial V} (p\boldsymbol{n} - \nu\rho\nabla\boldsymbol{u} \cdot \boldsymbol{n}) dS + \int_V \boldsymbol{F} dV \tag{3.2}$$

Numerical discretization

The equations are discretized for time and space. The time derivative is discretized using the forward Euler method, leading to the first-order accuracy. Space derivatives are discretized on a fixed Cartesian grid with staggered variables [82]. A staggered grid stores the scalar variables at the cell centres, and the velocity or momentum variables at the cell faces [34].

VOF is an efficient free surface modelling method for complicated free boundary configurations [37]. The VOF method consists of a scheme to locate the surface, an algorithm to track the surface, and a means of applying boundary conditions at the surface [27].

The nonlinear convective term is discretized with an upwind method. The method is only first-order accurate, and thus can not capture all flow phenomena well [43]. For flow around cylinders, vortex shedding will most likely not be accurate, or vortex shedding might not occur at all in simulations using this scheme [28]. Due to this, the simulated resistance can be inaccurate. This inaccuracy is dependent on the grid size, with smaller grid sizes, more accurate results are expected to be found. The advantage of first-order upwind discretization is that it is stable for convection dominated flows.

3.2. Simulation setup

The basic experimental setup is modelled in ComFLOW, with a cylinder of 0.4 m diameter and an underwater length of 0.5 m. The domain is smaller than the towing tank to minimize computing time, but still large enough to simulate the wake, the flow around the end, and the flow in front of the cylinder and to the sides of the cylinder. The simulations are 3D, without a turbulence model. The choice is made to not use a simulations method with turbulence model as these are still problematic, as discussed in paragraph 1.1.5. Table 3.1 shows the number of cells, domain dimensions, the discretization method for the convection term and the simulated length of time of the simulations. ComFLOW modifies the time step to conform to the Courant-Friedrichs-Lewy (CFL) limit, this timestep is thus not constant and will be smaller for finer grids. The grid used for the simulations is shown in figure 3.1. At the inflow, a velocity boundary condition (52 in ComFLOW) is used. At the outflow, a generating and absorbing boundary condition (11 in ComFLOW) based on the Sommerfeld boundary condition is implemented [88]. In ComFLOW an object is modelled by determining if cells of the Cartesian grid are solid, partially filled or empty.

Table 3.1: Computational details of the simulations

Program	**Number of cells (x, y, z)**	**Grid type**	**Domain (L, W, H) [m]**	**Waterdepth [m]**	**Convection Term**	**Run time [s]**	**Wave model**
ComFLOW	300 x 75 x 63	Cartesian	12 x 3 x 2.5	1.5	Upwind	2.5	Airy

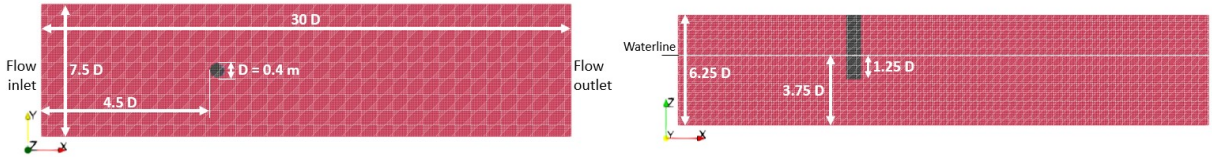

Figure 3.1: Top and side view of grid with dimensions, black indicates the location of the cylinder within the grid

Simulations with a varying number of cells, underwater length of the cylinder, flows and height of the upper boundary are conducted. The values are shown in table 3.2. These variations allow for a study into grid refinement, end effects and free surface effects. By placing the upper boundary of the flow below the free surface, effectively no free surface will be simulated. Similarly, an underwater length of the cylinder of 1.5 meters until the bottom of the domain will lead to no free end and thus no end effects being simulated. The results of the simulations after 1 second were used, to allow the simulation to initially stabilize. The simulation starts with an approximated velocity field that does not satisfy the boundary conditions yet. This causes a disturbance that needs to settle before the output can be trusted. As stated in paragraph 4.4.1, it is found that a time of more than the simulated time is needed to eliminate all start-up effects.

Table 3.2: Grid sizes, lengths, flows and free surface effects tested with simulations

Number of cells	90 000	307 800	1 417 500	3 880 800	8 237 700	
Underwater length cylinder [m]	0.5	0.75	1	1.25	1.4	1.5
Current [m/s]	0.88	4.02				
Wave period [s]	-	1.48				
Wave height [m]	-	0.14				
Free surface effects	yes	no				

4

Results

The goal of this research is to find C_D and C_M of a surface piercing cylinder in flow with high Reynolds and low Keulegan-Carpenter numbers and to investigate the drag force on such a cylinder. The results of the experiments are evaluated and discussed in this chapter.

4.1. Comparing to previous research

A deliberate overlap with existing research was made to be able to compare to previous research. Figure 4.1 shows data from previous research, compared to the results of experiments in a steady current. When evaluating the results it is found that the data is similar to that of previous researchers, but not identical.

Firstly, the values for C_D found in the current research are lower for subcritical ranges of Re. Chaplin et al. and Hay's [17] research was conducted with a vertical surface piercing cylinder with a length over diameter ratio of 2 and Fukuoka et al. [29] with a ratio of 1.25, both larger than the 1.21 in the current research. It is likely the cause of the difference, as the cylinder is short for its diameter, and this is found to lead to lower values of C_D in a similar range of Reynolds numbers [29].

A second difference between previous research and the current research can be found when observing the trend of the data. The value for C_D from the current research seems to decrease at $7{\cdot}10^5$, where for the previous research, this happens between Reynolds numbers of $2{\cdot}10^5$ to $4{\cdot}10^5$. When comparing this to literature [67], it is found that this could indicate the cylinder in the current research being smoother than the cylinders in the previous research, as the transition period is found at higher Reynolds numbers. This could not be verified.

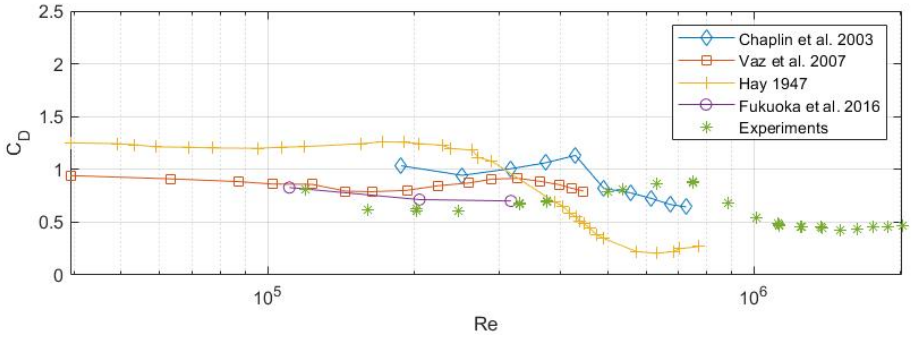

Figure 4.1: Additional measurements of current research compared to previous research [17, 29, 49]. The dependency of C_D on Re in a steady current is shown

Next, we compare the results from tests in flow and waves to previous research. Due to the size of the cylinder, an overlap with previous research could not be made. In figure 4.2 a comparison is made with previous research also on surface piercing cylinders [60, 92]. However, this research is at different Reynolds numbers. There is also no overlap for KC, so evaluating the current research in this figure is difficult. However, the results from the experiments are in line with the previous research, especially since for a Reynolds number closer to the previous research, the drag coefficient becomes more similar.

It is thus concluded that the results from the experiments be trusted.

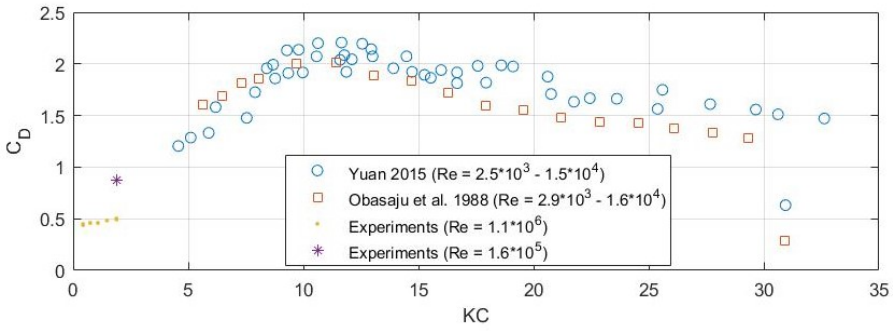

Figure 4.2: Current research compared to previous research [60, 92] at Re $< 1.1 \cdot 10^4$. The dependency of C_D on KC is shown. Note the different values of Re. One run is conducted at a Re = $1.6 \cdot 10^5$ to bridge the gap with previous research

4.2. Coefficients

Figures 4.3 and 4.4 show the resultant C_D and C_M for the experiments conducted for the values shown in table 2.1. Evaluating the results, it is found that C_D varies between 0.4 and 0.5 for all combinations of KC and Re. C_M varies between 0 and 3.5. The values of C_D and C_M set out against KC are for various Re values, and vice versa for the right figure. As the spread of data is larger when plotted against KC compared to it being plotted against Re for C_D it can be concluded that C_D is more strongly dependent on Re than KC for the given range.

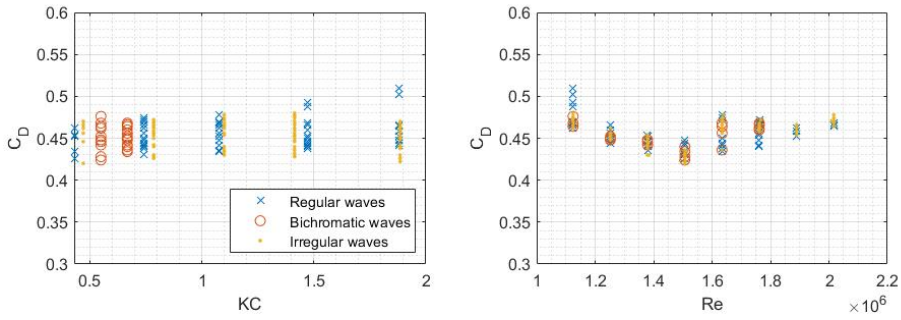

Figure 4.3: C_D found from the experimental data, its correlation to KC and Re shown

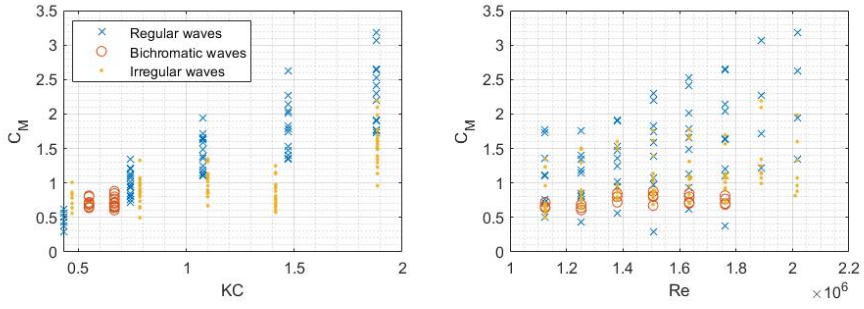

Figure 4.4: C_M found from the experimental data, its correlation to KC and Re shown

The values of C_D and C_M for all three wave types have also been set out against β, shown in figure 4.5. This visualization allows for the dependency of C_D and C_M on both KC and Re to be evaluated in one figure. The figure shows that for lower values of β, thus for relatively larger values of KC compared to Re, C_D increases. For C_M a large spread is found. The results also show an increase for lower values of β.

To find more detailed results, the different types of waves have been separated and the different values of KC are differentiated. The results are shown in figure 4.6. Firstly, it shows a repetitive pattern for the various values of KC. As this pattern is found at constant KC, it must indicate the effect of Re. Secondly, it can be found that for regular waves, C_D increases with KC. This is not found for irregular waves. It is thought that as it is a wave spectrum, the effect of increased wave height is lost in the great variety of wave components.

For C_M it is found in figure 4.4 that its values strongly dependent on KC and Re for regular waves, as C_M increases for both. For irregular waves, similar to C_D, no such clear conclusion can be made. Interesting about the values of C_M is that values larger than the theoretical maximum of two are found [44]. This theoretical maximum is determined without free surface effects and does not include the difference in the water column at the cylinder due to waves. The moment the cylinder is between a peak and through, there is a difference in height of the water between the front and back of the cylinder. This is in phase with the acceleration in the wave and is thus included in C_M. For the largest wave tested with a period of 2 s and a height of 0.24 m, it is calculated that the theoretical maximum for this specific setup is 6.6. These are estimations but show that a value of 3.5 is not unreasonable when free surface effects are included.

Due to the chosen experimental setup, the application point of the drag force is also known. The results are shown in figure 4.7. d_F is the application point measured from the bottom of the cylinder. d_F was found to be on average 0.29 m above the bottom of the cylinder. This is above the middle of the underwater length of the cylinder, indicating that the average force is not spread equally over the length. For Reynolds numbers below $1.5{\cdot}10^6$, the application point is at the middle of the cylinder. This means that the forces that act in the top half of the cylinder are probably negated by a force on the lower half of the cylinder. For higher Reynolds numbers, d_F increases tot 0.33 m from the bottom, 69% of its underwater length. No clear dependencies on KC were found.

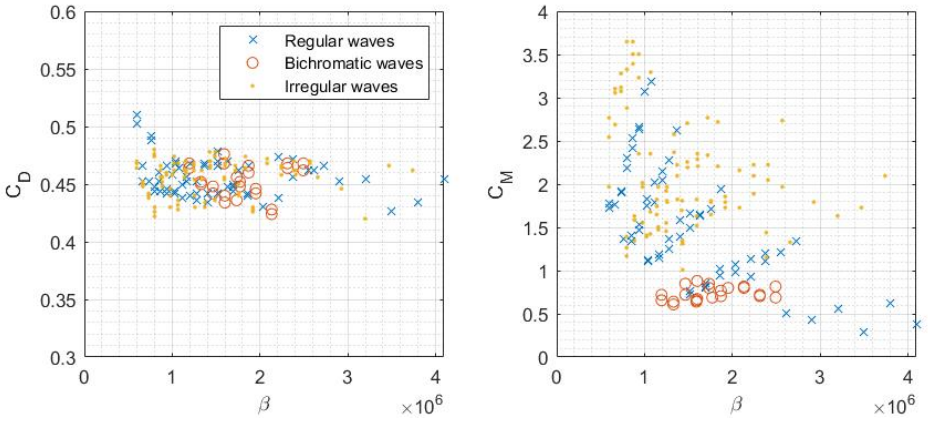

Figure 4.5: C_D and C_M found from the experimental data, plotted for β. Note the different scale of the y-axis

Summary

It is concluded that C_D varies between 0.4 and 0.5 in the range tested including waves. For C_M values between 0 and 3.5 were found. Both depend on both Re and KC. Regular waves showed a stronger dependence on KC compared to their irregular counterparts with a peak frequency equal to the regular wave frequency. This, as well as the values of the coefficients being different, shows that the coefficients found for regular waves are not applicable for irregular waves for the same KC and Re. The application point of the drag force is in the middle of the underwater length of the cylinder for Re < $1.5{\cdot}10^6$, and for larger values above the middle.

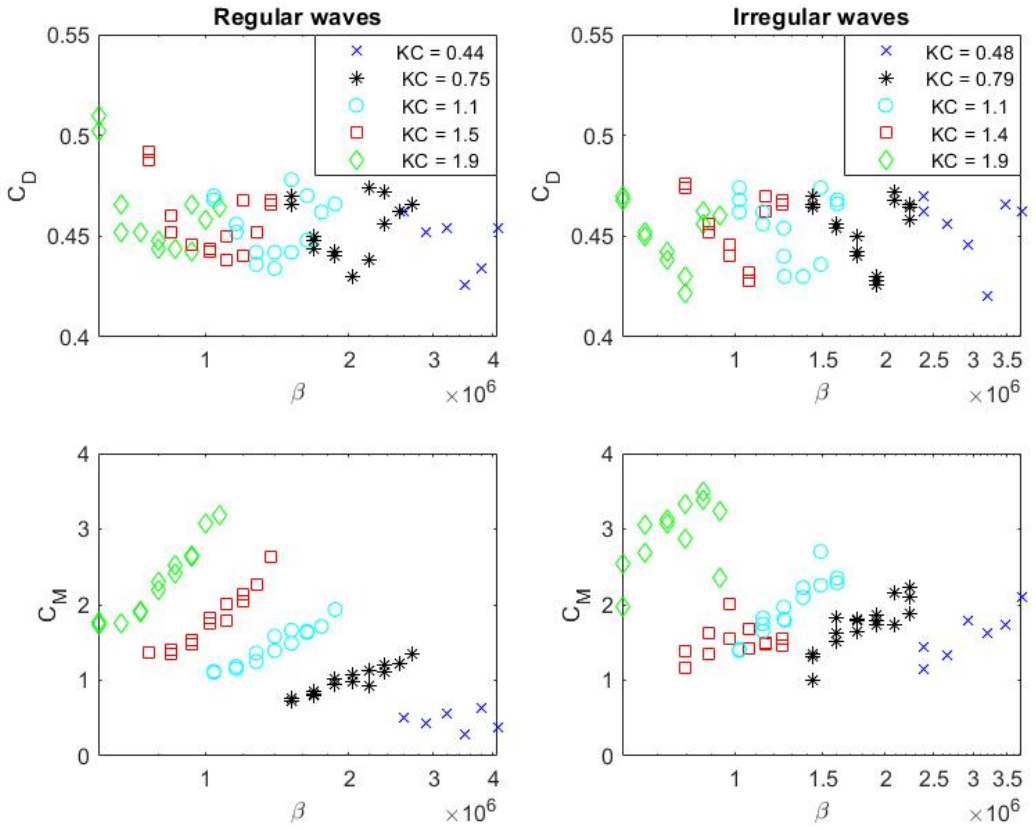

Figure 4.6: C_D and C_M found from the experimental data, plotted for β. Wave types are shown separately and different KC values are made identifiable, showing the dependencies on Re and KC more clearly. Note the different scale of y-axis

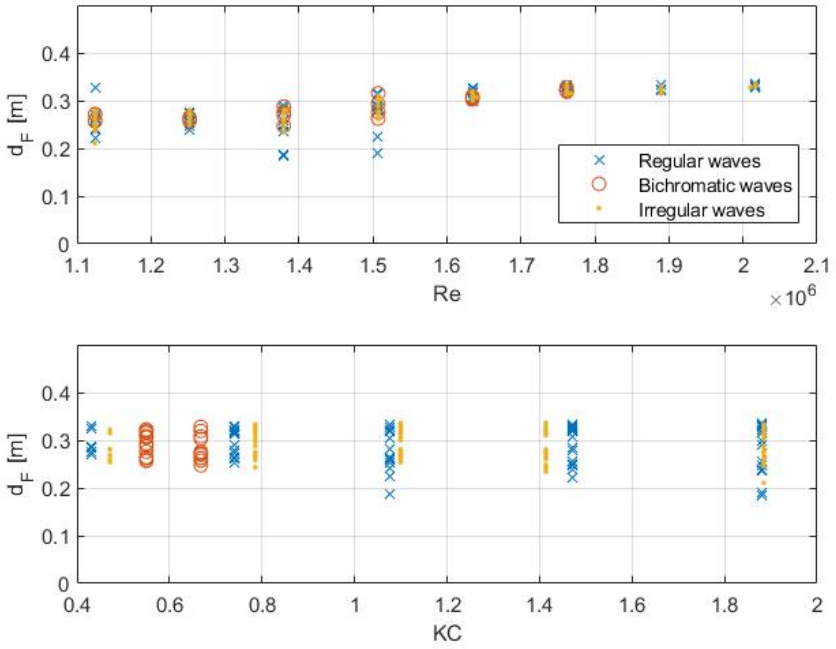

Figure 4.7: Distance to the application point of the drag force (d_F) measured from the bottom of the cylinder for Re and KC. The spread shown in both is due to a variation over the range of respectively KC and Re

4.3. Analysis in frequency domain

By evaluating the measured forces in the frequency domain, a better understanding of the different hydrodynamic phenomena can be obtained. The sampling rate during testing was 1000 Hz and the data is filtered at 100 Hz.

Sources of periodic forces

The vortex shedding frequency is estimated using the Strouhal number (St). St of 0.2 and 0.5 is expected for Reynolds numbers in the tested range for a smooth cylinder in a steady flow. The effects of waves on these values are difficult to quantify due to flow reversal [76].

The load cells through which the cylinder is fastened are practically stiff springs. Natural frequencies of the system can influence the data due to resonance with periodic forces and frequency lock-in. Through excitation tests, the natural frequencies are found to be 10 to 11 Hz and at 15 to 16 Hz.

Previous research has shown that higher harmonic forces might occur during the experiments [31, 65]. Ringing has been found to affect surface piercing cylinders in waves. These ringing responses occur during high sea-states. At these high sea states, the wavelength is longer than ten times the diameter and the wave height is comparable to the cylinder diameter. In experiments with similar values [31], a second-order harmonic suction force due to free surface effects was found. Ghadirian and Bredmose [30] found that secondary load cycle is confined from just above still water level to 1.5 times the cylinder diameter below the still water level. This is the range in which the cylinder in the experiments is situated.

The test setup is placed within a larger setup: the towing tank carriage. In the force measurements at velocities below 1 m/s, a periodic force equal to a rotation of the wheels of the carriage was found, implying a possible imperfection on the wheels. The effect of this during higher velocities is not clear, but no frequency equal to the frequency of the rotations of the wheels was found when analyzing the test data.

Data analysis

Figures 4.8, 4.9, 4.10 and 4.11 show the frequency components found using a Fourier transform of the force measurements. In these figures also the expected frequencies of possible sources of the periodic forces are indicated. Possible sources in figure 4.8 are the double vortex shedding frequency and the natural frequencies. The vortex shedding frequency is shown as twice as high as the vortex shedding cycle includes two vortexes, 180° out of phase, thus inducing double the periodicity in the drag direction.

In figure 4.8 it is shown that it is likely that vortex shedding occurs and that the effect is intensified by the natural frequencies of the experimental setup. This is most prominent at Reynolds numbers above $1.5{\cdot}10^6$ and frequencies of 7 to 10 Hz.

In the figure frequencies with a significant force amplitude between 12 and 20 Hz were found. These frequencies were found for all flow types. The source is unknown, but it is most likely caused by the carriage of the towing tank and is thought to not be a hydrodynamic effect.

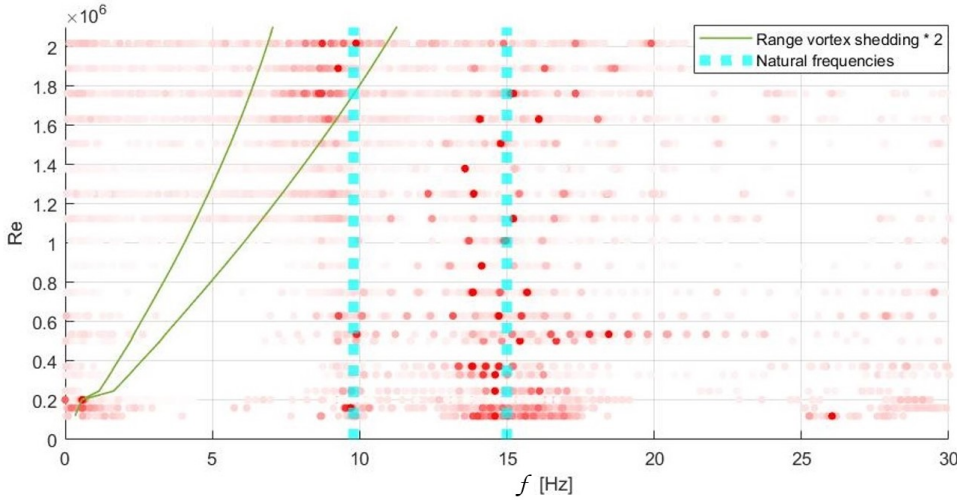

Figure 4.8: Frequencies found during tests without waves with likely sources of periodic forces indicated. Brighter red indicates a higher amplitude compared to the maximum amplitude per value of Re

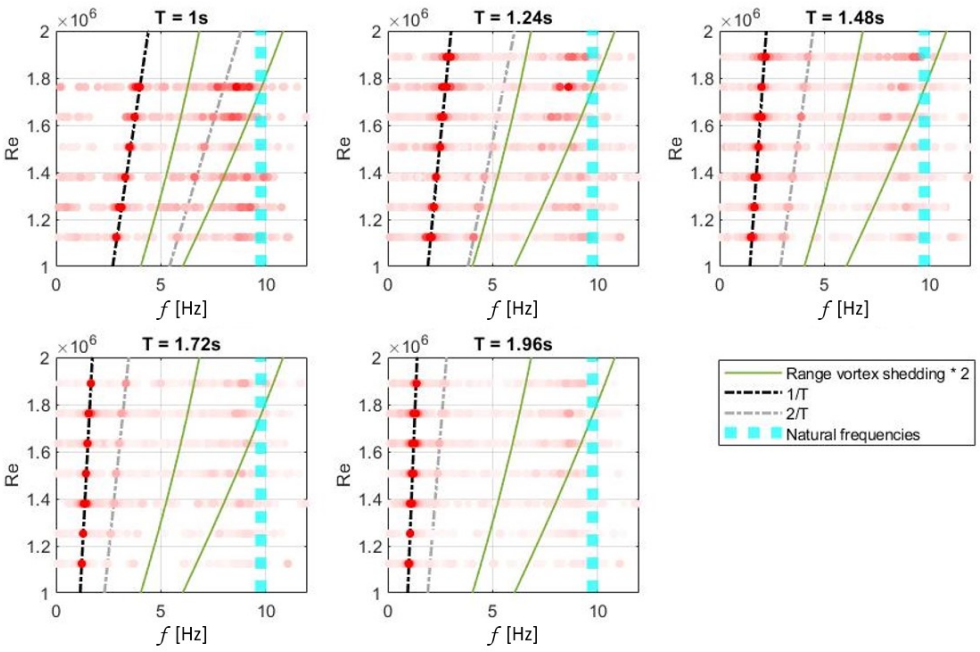

Figure 4.9: Frequencies found during tests with regular waves with likely sources of periodic forces indicated. Brighter red indicates a higher amplitude compared to the maximum amplitude per value of Re. The colour of the amplitudes is enhanced by a factor two. Wave frequencies are adjusted for the Doppler effect

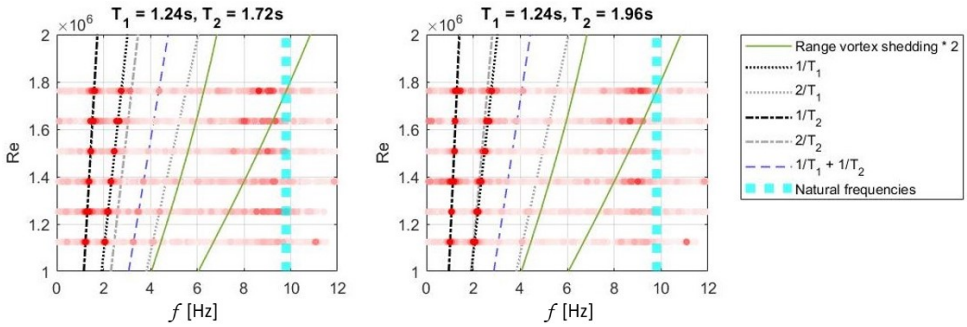

Figure 4.10: Frequencies found during tests with bichromatic waves with likely sources of periodic forces indicated. Brighter red indicates a higher amplitude compared to the maximum amplitude per value of Re. The colour of the amplitudes is enhanced by a factor two. Wave frequencies are adjusted for the Doppler effect

In figure 4.9 the frequency components found from the force measurements using a Fourier transform are shown. The figures show, in addition to the possible sources shown in figure 4.8, the wave frequency and the double wave frequency, both adjusted for the Doppler effect, leading to the slopes found in figures 4.9, 4.10 and 4.11. The double wave frequency indicates second-order effects. It should be noted that slight non-linearity in the waves, due to the wave steepness, might have increased the force with double the wave frequency. After analysis, it is concluded that the non-linearity does not account for the majority of the found force amplitude, as discussed in paragraph A.5.1.

Figure 4.9 shows, as expected, that the waves are the dominant source of periodicity. The figures again show that vortex shedding occurs and is amplified when closer to the natural frequencies, signifying frequency lock-in. For the longer wave periods, this becomes less significant compared to the maximum force amplitude, as the maximum force amplitude increases.

The frequencies for bichromatic waves have similarly been analyzed, shown in figure 4.10. In the results the wave encounter frequency is again found for the bichromatic waves, but no clear evidence of higher-order harmonic forces of the waves are found. There is, however, a small force component with the combined frequency of the two waves.

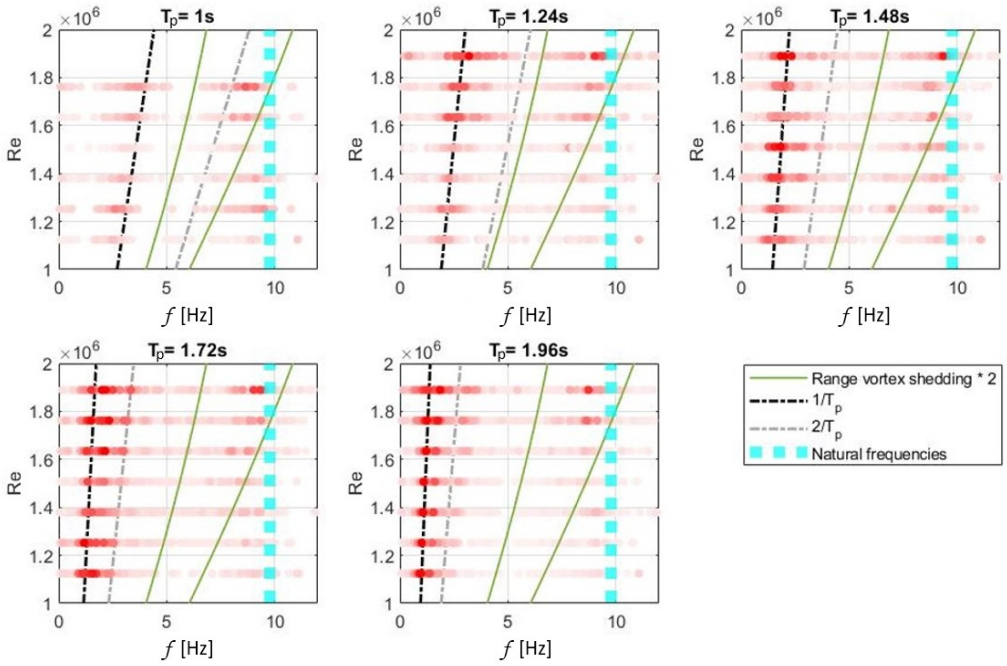

Figure 4.11: Frequencies found during tests with irregular waves with likely sources of periodic forces indicated. Brighter red indicates a higher amplitude compared to the maximum amplitude per value of Re. Wave frequencies are adjusted for the Doppler effect

Lastly, the periodic forces found for the irregular wave experiments are analyzed and visualized in figure 4.11. The figures show a spread of frequencies around the peak frequency, as is expected for a wave spectrum. No higher-order harmonic wave forces were found. Frequencies between 8 and 10 Hz were found similar to those in figures 4.8, 4.9 and 4.10, making it likely that these frequencies are indeed due to vortex shedding.

Force amplitudes as a percentage of the average total force are shown in table 4.1 to quantify what is shown in the previous figures. Shown is the sum of amplitudes found within the range of frequencies where certain effects are expected. It should be noted that this is thus the maximum possible amplitude, so for sources spread over a range of frequencies, the amplitude is overestimated. Vortex shedding is close to the natural frequency for Re $> 1.5 \cdot 10^6$, thus the amplitude of the force due to vortex shedding could be increased due to frequency lock-in.

Table 4.1: Average maximum amplitude of the forces due to identified sources of periodic forces, as a percentage of the average total force

	Regular	Bichromatic	Irregular
First-order wave	49%	44%	321%
Second-order wave	7%	-	-
Vortex shedding	32%	34%	37%
Wave-wave interaction	-	23%	-

Summary

From analyzing the forces in the frequency domain it is observed that for Reynolds numbers above $1.2 \cdot 10^6$ vortex shedding occurs for all flow combinations. The results indicate that the vortex shedding has locked-in with the natural frequency. For regular waves, second-order harmonic wave forces were identified. For bichromatic waves, a periodic force with a frequency equal to the summation of the wave frequencies is found.

4.4. Simulations

The results of the simulations discussed in chapter 3 are analyzed to evaluate the simulation methods capability of accurately simulating the problem. After this, results with regards to the effects of the free surface and end effects of the cylinder on the drag are discussed.

Figure 4.12: Simulated free surface in blue and cylinder in yellow at t = 2 s, with U = 4.02 m/s and regular waves with T = 1.48 s and H = 0.14 m

4.4.1. Simulation quality

Figure 4.12 shows a realistic-looking simulated free surface. However, when looking at figure 4.13, it becomes clear that there are some problems with the simulations. These figures show the pressures in the flow. In the experimental results, periodic forces in the force measurements indicated vortex shedding occurring [10]. Looking at these pressure distributions it is clear that vortex shedding is not simulated, and this was verified by analyzing the results in the frequency domain. This is because the simulated time is too short. A simulation with a simulated time of 30 seconds with a flow velocity of 4.02 m/s and a wave period and height of respectively 1.48 s and 0.14 m was run. This simulation does simulate vortex shedding. This vortex shedding has a lower amplitude and frequency as was found in experiments. For the simulation a Strouhal number of 0.25 was found, while for the experiments numbers for the same flow a Strouhal numbers of about 0.42 are found. The difference between simulated and actual vortex shedding is expected and explained in chapter 3. Simulations long enough to simulate vortex shedding take over five times the calculation time. C_D and C_M found from the simulation including vortex shedding are 5% higher than C_D and C_M found from simulations without vortex shedding. This is likely because the boundary layer is not fully formed for the shorter simulations, also causing the lack of vortex shedding. The simulations of 30 s take 5 times the calculation time, while leaving a systematic error as viscous effects are still not accurately modelled. Because of this, the choice was made to not lengthen the simulation time.

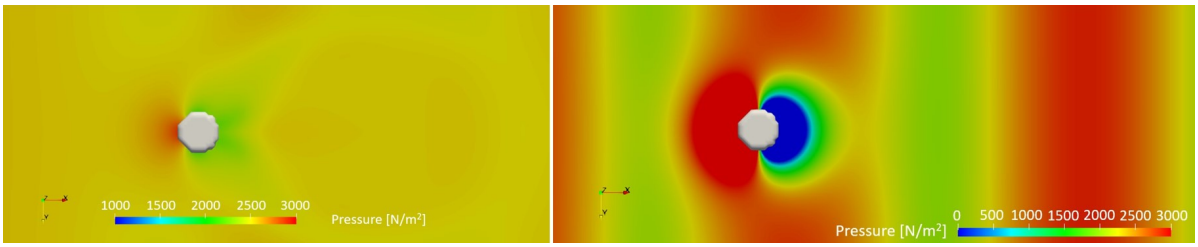

Figure 4.13: Pressures at z = 1.25 m and t = 2 s. On the left an underwater length of the cylinder of 1.5 m, with U = 0.88 m/s and no waves. On the right an underwater length of the cylinder of 0.5 m, with U = 4.02 m/s and regular waves of T = 1.48 s and H = 0.14 m. Flow in positive x-direction

In general, it is found that for finer grids, more accurate results are obtained. However, this is not always the case. For the grid refinement study in figure 4.14 results varying greatly from results with coarser grids are found. When calculated force and free surface were analyzed it was found that this grid leads to unstable simulations. This can be caused by numerical damping being small for such a fine grid, thus the spatial discretization is not stabilized as much as for courser grids, leading to unstable simulations [84].

4.4.2. Surface and end effects

Figure 4.14 shows a grid refinement at Re = 2.8 $\cdot 10^5$, the first flow described in table 3.2. A grid refinement study is conducted for a cylinder with a length of 1.5 m, and thus no end effects are included. The figure also shows simulations with the upper boundary below the free surface, eliminating free surface effects. These simulations are compared to a grid refinement study which includes both surface and end effects, as was also the case in the experiments. It is compared to literature [17, 49]. It is found that end effects decrease C_D. Free surface effects slightly increase C_D. For all the grid refinements in figure 4.14, C_D goes to a value slightly lower than the values of C_D found in previous research. This is surprising as it is known that most modelling methods overestimate the drag on a cylinder [2]. It can be caused by the underdeveloped boundary layer, as paragraph 4.4.1 shows that if vortex shedding is simulated C_D can increase with 5%. The results from the finest computed grid, with 8.2 million cells, does show a higher C_D. However, when calculated force and free surface were analyzed it was found that this grid leads to unstable simulations. This is explained in paragraph 4.4.1.

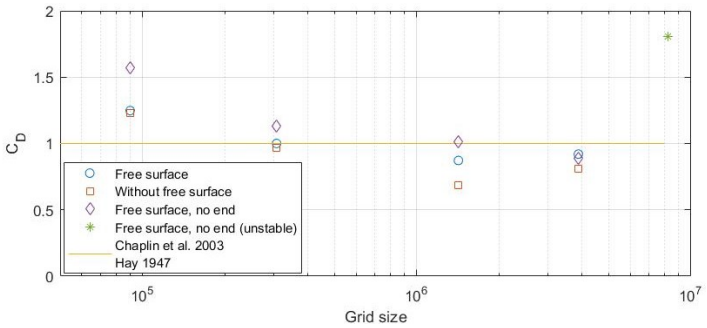

Figure 4.14: Results for C_D from simulations with and without free surface effects and with and without end effects compared to previous research [17, 49], for U = 0.88 m/s or Re = 2.8 $\cdot 10^5$

Estimations based on literature

As stated previously, free surface and end effects will influence the results of the experiments. Using literature, their influence is estimated. The goal is to investigate how these effects influence the results.

Due to scaling and the focus on the Reynolds numbers, the experiments were conducted at high Froude numbers of 1.5 to 2.4, while for energy generating devices Fr = 0.05 - 0.24. This large discrepancy is a point of interest, as it will influence C_D.

The free surface estimations are made based on the research by Chaplin and Teigen [17], which considers surface piercing cylinders with a length over diameter of 2 in a flow with only current, up to Reynolds over Froude number (Re/Fr) of 3$\cdot 10^5$. This Re/Fr is lower than the values found in the current research (Re/Fr = 6.47 $\cdot 10^5$ - 8.4 $\cdot 10^5$). These results are used due to a lack of other options. As there are numerous differences between the previous and current research, the estimations are not expected to be accurate. The results are shown in figure 4.4.2, which shows the average measured force for all experiments dependent on the Reynolds number, and the estimated average force if there was no free surface.

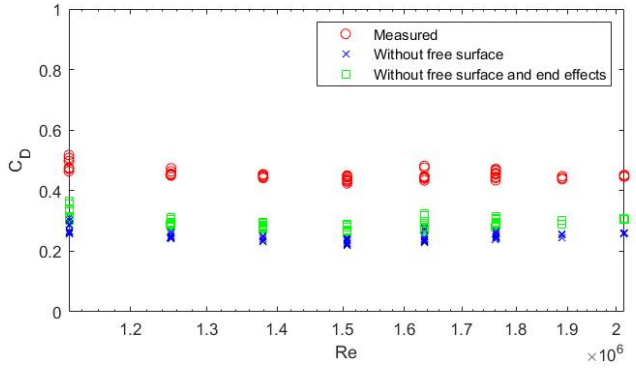

Figure 4.15: Estimated based on literature [17, 29] for the influence on free surface and end effects on C_D

The influence of the end effect depends on the length over diameter ratio. For a length over diameter ratio of around 1.25 or larger, C_D will increase for larger values of Re, as is discussed in paragraph 3. Using the results found in Fukuoka et al. [29] an increase of 7.7 % in C_D at a five times increase in length over diameter ratio is found, from 0.25 to 1.25. These length over diameter ratio's are smaller than those of the cylinder from the simulations, and thus these estimates are not expected to be accurate.

Including both the estimations for the influence of the free surface, as well as the influence of the end effects, C_D without free surface and end effects is estimated and shown in figure 4.4.2. As there was no research found at similar ranges as the current research, the results of the estimations shown in figure 4.4.2 could not be validated. The results are compared to the results from the simulations in figure 4.16. They both show that free surface effects cause C_D to increase while eliminating end effects causes an increase in C_D. However, the estimation based on literature shows a much larger decrease when eliminating surface effects than the simulations shown in figure 4.16. Likely, the values used from previous research are not usable due to the differences between the current and previous research. Thus, the simulations should be considered as the more accurate results. Note however that, as was stated in paragraph 3, these do not accurately model viscous effects which can influence the results.

4.4.3. Free surface

Another grid refinement study for the second flow in table 3.2, is shown in figure 4.16. Here C_D gets close to a value slightly above the value found in experiments. The simulations were with a modelled cylinder underwater length of 0.5 m, as were the experiments of which the results are shown in the figure. The figure also shows simulations without free surface effects. It is found that without free surface effects, C_D decreases slightly. This is because free surface effects allow for wave making and breaking resistance to occur, increasing the drag.

The right figure of figure 4.16 shows that C_M is somewhat accurately modelled when the free surface is taken into account. Without the free surface effect, however, it is found that the forces are lower. This is expected as the difference in free surface elevation is maximum in the phase with the horizontal wave acceleration thus the forces due to the free surface elevation are captured in C_M, as is explained in paragraph 4.2. Without free surface effects, C_M should not go above the theoretical value of 2, which it indeed does not do.

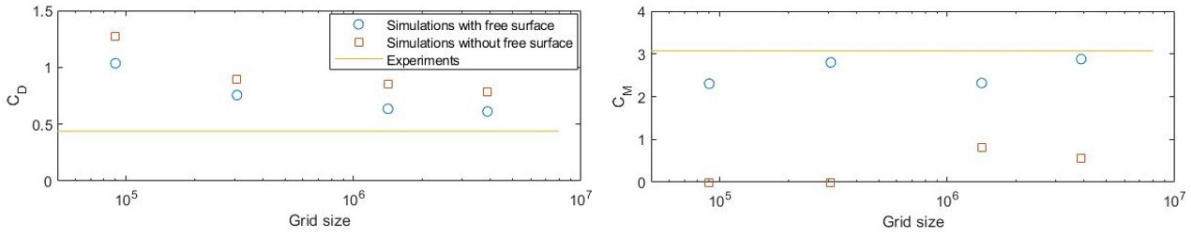

Figure 4.16: C_D and C_M obtained from grid refinement study with U = 4.02 m/s and regular waves with T = 1.48 s and H = 0.14 m, simulated with and without free surface

Froude scaling

Free surface effects can be considered to scale differently than the viscous effects as they scale with the Froude number (Fr), shown in equation 4.1, in which g is the gravitational acceleration.

$$Fr = \frac{U}{\sqrt{D \cdot g}} \tag{4.1}$$

Due to scaling and the focus on the Reynolds numbers, the experiments were conducted at high Froude numbers of 1.5 to 2.4, while for energy generators Fr = 0.05 - 0.24. This large discrepancy is a point of interest, as it can influence C_D. Previous research has found that the free surface effects increase C_D [17], as was found with the simulations. By keeping $U \cdot D$ constant by multiplying the D with a value and dividing U by the same value, a constant Reynolds number and a varying Froude number can be found. The used values are shown in table 4.2. The simulations did not include waves.

Table 4.2: Simulated diameters and velocities and the resulting values for Reynolds and Froude numbers tested

D [m]	0.4	0.8	1.6			
U [m/s]	0.88	0.44	0.22	4.02	2.01	1.01
Re	$3.3 \cdot 10^5$	$1.5 \cdot 10^6$				
Fr	0.055	0.156	0.44	0.253	0.718	2.03

The results are shown in figure 4.17. The results from the simulations are in a similar range to the experimental results from the previous research by Ducrocq et al. [25]. In paragraph 3 it is found that viscous effects are not correctly modelled by the simulations, and it is possible that because of this, even though the Reynolds number is kept constant, the viscous effects are not constant. The results can thus not on themselves be used to conclude the effects of the free surface.

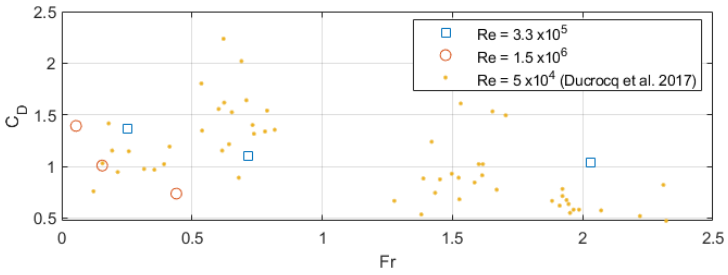

Figure 4.17: C_D found through simulations at various Froude numbers for constant Reynolds numbers compared to experimental results from previous research [25]

4.4.4. Geometry and end effects

In the figure 4.18 the results for lengthening the cylinder are shown for a flow with Re = $2.8 \cdot 10^5$, the first flow described in table 3.2, making it comparable to previous research. The figure shows that for a longer length cylinder, C_D increases. This is in line with previous research [29], which indicates that lengthening of the cylinder causes a reduction of pressure recovery from flow around the end of the cylinder. C_D from the simulations seems to get closer to 1: the coefficient found in previous research of Chaplin and Teigen [17] and Hay [49], which tested a length over diameter ratio of 2. When the cylinder is made longer than the modelled domain, and thus no end effects are taken into account, C_D becomes larger than 1. This underlines the theory of Fukuoka et al. [29], that C_D will increase for larger length over diameter ratio's, as pressure recovery from re-circulation is reduced.

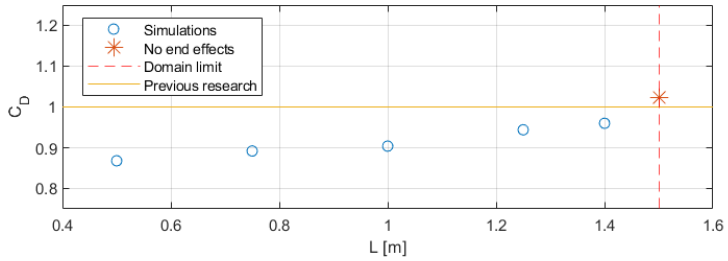

Figure 4.18: Influence of aspect ratio of the cylinder on C_D, with U = 0.88 m/s and no waves, grid of 1 417 500 cells, compared to previous research [17, 49]

Summary

It is concluded that the simulations do not accurately model vortex shedding within the modelling time used in this research, but do accurately model the forces from free surface effects. From grid refinements studies it is found that they do give results for C_D and C_M accurate enough to be able to find some conclusions. It is found that a longer cylinder length increases C_D. Eliminating free surface effects decrease it. This is also found from estimations based on literature. Simulations show that C_M increases due to free surface effects.

4.5. Evaluating Morison equation

The Morison equation is used for force calculations. This also includes calculations for fatigue limit states [23]. This is why in this paragraph the Morison equation is assessed in the time and frequency domain.

Time domain

As shown in table 2.3, the Morison equation does not perfectly simulate the measured force. As was discussed in paragraph 2.4, this can be caused by small phase shifts in estimating the flow velocities, as well as additional frequencies being measured which are not caused by hydrodynamic effects. However, a difference between Morison and measured force was also found in the frequency domain. In paragraph 4.3 it is revealed that an additional frequency was measured that was likely caused by the carriage of the towing tank, and thus not a hydrodynamic effect. Forces with this frequency are filtered from the measurements for the results in this paragraph, using frequency selective filtering in the frequency domain [4]. The coefficient of determination (R^2) in the time domain is used to find how well the Morison equation fits the measurements.

Figure 4.19 shows that the accuracy of the Morison equation depends strongly on the KC value. On average an R^2 value of 59% was found between the Morison result and the measured force, meaning that a variance of 41% is not accounted for. It is more accurate for regular waves with an averages R^2 of 72%. For bichromatic waves (R^2 = 57%) and irregular waves (R^2 = 48%) it isn't as accurate. This could be because the description of the flow is less accurate for irregular and bichromatic waves. For values of R^2 it should again be noted that phase changes, as the evaluation is in the time domain, and higher frequencies due to noise can decrease the R^2 value. Noise will have more influence for lower waves as these cause smaller force amplitudes, possibly explaining the dependency of R^2 on KC. Figure 4.19 shows that for KC > 1, R^2 > 50%, compared to $R^2 \approx 30\%$ for KC = 0.44. Equation 1.3 is also significantly better at modelling forces resulting from regular waves compared to those in irregular waves. By analyzing the flow components an understanding of the inaccuracies of the Morison equation can be obtained.

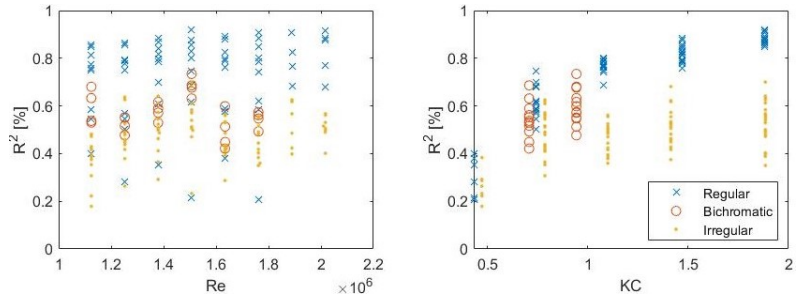

Figure 4.19: Accuracy of Morison equation compared to the measured force for all experiments, represented by R^2 and shown for Re and KC

Frequency domain

As discussed, the accuracy with which the Morison equation models various periodic forces is of importance for fatigue calculations. The periodic forces measured are discussed in paragraph 4.3. It is found that the Morison equation underestimates second-order wave forces and wave-wave interaction and Morison does not model vortex shedding. This is visualized in figure 4.20.

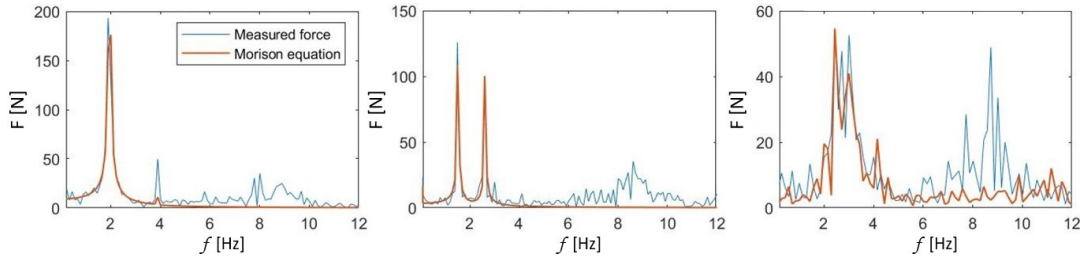

Figure 4.20: Difference between force found with Morison equation and measured force, shown in the frequency domain. Note the different scale of y-axis. Left: regular waves with T = 1.48 s and U = 4.36 m/s, Middle: bichromatic waves with T = 1.24 and 1.72 s and U = 4.36 m/s, Right: irregular waves with T_p = 1.24 s and U = 4.7 m/s. The values at 0 Hz are not shown

To quantify this inaccuracy the modelling of the forces for bichromatic waves is set out for the identified periodic forces, as discussed in paragraph 4.3. Figure 4.21 shows the relative error between the measured force and the force estimated with the Morison equation. f_1 and f_2 indicate the frequencies of the two waves in the bichromatic wave. The figures show that constant drag force due to current is accurately estimated, but the first-order wave forces less so. Wave-wave interaction and second-order wave forces are modelled between 50 to 100% lower than their measured values. This is most likely due to the current being the main source of drag, and thus the coefficients being tuned to model it correctly, and as the same coefficients are used to model all other sources of forces, these are not estimated as well.

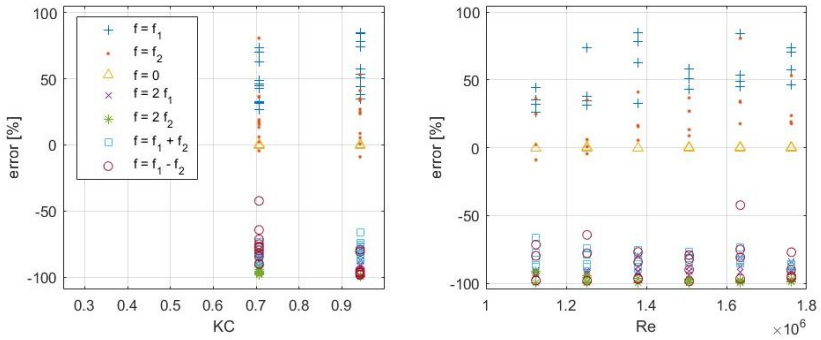

Figure 4.21: Error between the measured force amplitude and the force amplitude calculated with the Morison equation for the identified force frequencies for bichromatic waves

Three-term Morison equation

As stated in paragraph 1.1.2, a three-term Morison equation can also be used in research. The three-term Morison equation can not be used for bichromatic and irregular waves, and thus the classical Morison equation is used in this research.

For regular waves, the three-term Morison equation is evaluated. This is to find if the inaccuracies found can be solved with this equation. The equation is shown in equation 4.2. In this equation, ω is the angular wave frequency.

$$F_{comp} = \frac{1}{2} \cdot \rho \cdot D \cdot L \cdot C_D \cdot U_c |U_c| + \frac{1}{2} \cdot \rho \cdot D \cdot L \cdot C_D \cdot U_m^2 \cdot cos(\omega \cdot t) |cos(\omega \cdot t)| + \frac{1}{4} \cdot \pi \cdot \rho \cdot D^2 \cdot L \cdot C_M \cdot \dot{U} \tag{4.2}$$

The coefficients used in the three-term Morison equation are obtained from the experimental runs including either regular waves or current. In previous research, it has been the case that the LS or LSFD method was applied using the three-term Morison equation. The extra variable lead to improved fitting to the force and thus better results. This method is thought to be problematic as it does not lead to results which can be used to predictive modelling of the forces, as discussed in paragraph 1.1.7. This is why previously found coefficients are used in this research.

It is found that the three-term Morison equation models with an average accuracy of R^2 = 59%, a lower value than the R^2 = 72% from the classical Morison equation. As the classical Morison equation is used in the LS and LSFD method, the results are optimized for this equation and not the three-term Morison equation, possibly explaining the large difference. However, it is shown that the three-term Morison equation is not preferable for this experimental setup.

Summary

The Morison equation can model flows with regular waves fairly well. However, problems arise for different flows. This is thought to be mainly caused by the Morison equation using only one C_D and C_M for all flow components, as well as not including vortex shedding and underestimating second-order wave forces and wave-wave interaction.

4.6. Rewritten Morison equation

In paragraph 4.5 problems are found with the Morison equation for flows with bichromatic or irregular waves. Irregular wave patterns are of interest as structures placed in oceans are subject to them. Paragraph 4.2 states that the coefficients found for regular waves are not applicable to wave spectra with a peak period equal to the wave period, making it more difficult to find the forces due to irregular waves. Besides this, it is theorized that the problems found are likely caused by using only one C_D and C_M for all flow components. It is theorized that the Morison equation can be rewritten, as shown in equation 4.3. The equation proposes using a different C_D and C_M for every wave from an irregular spectrum. In this equation $U_{tot} = \sum_{i=1}^{n} U_i$ and $\dot{U}_{tot} = \sum_{i=1}^{n} \dot{U}_i$. C_{D_i} and C_{M_i} are the corresponding coefficients to the flow described by U_i and $\dot{U}_i$.

$$\begin{aligned} F = \frac{1}{2}\rho DL \cdot C_{D_{tot}} \cdot U_{tot}|U_{tot}| + \frac{1}{4}\pi\rho D^2 L \cdot C_{M_{tot}} \dot{U}_{tot} = \\ \frac{1}{2}\rho DL \cdot sign(\sum_{i=1}^{n} U_i) \cdot (\sum_{i=1}^{n} \sqrt{C_{D_i}} \cdot U_i)^2 + \frac{1}{4}\pi\rho D^2 L \cdot \sum_{i=1}^{n} C_{M_i} \cdot \dot{U}_i \end{aligned} \tag{4.3}$$

Time domain

An irregular wave pattern is a summation of multiple regular waves. A bichromatic wave is a summation of two regular waves, and can thus be seen as a simple irregular wave pattern. The rewritten Morison equation is tested using bichromatic waves, as it has a more accurate and clear flow description. The coefficients for the combined flow are needed, as well as those for the current and waves separately. As the bichromatic waves have been modelled with wave components of a steepness half that of the regular waves, no direct corresponding coefficients are known. However, it is known that the coefficients depend on KC, thus coefficients are found by interpolating for coefficients of regular waves at similar KC values.

As is discussed in paragraph 4.5, the frequencies likely caused by the towing tank carriage are filtered from the data. Using the filtered data it is found that the rewritten Morison equation correlates with R^2 = 61%, with a variance of 0.6%, to the filtered measured data, and the classical method with R^2 = 57% with a variance of 1%. It should again be noted small phase shifts and higher frequencies will cause R^2 to be lower. It is promising that a higher value of R^2 is found, as the LSFD method is used with the classical Morison equation, thus optimizing the results, in contrast to the rewritten equation. The results agree with the theory that the forces in irregular waves can be better modelled using the rewritten Morison equation.

Frequency domain

The rewritten Morison equation is also analyzed in the frequency domain. Using the knowledge of the periodicity of the flow effects, combined with the written out rewritten Morison equation, allows for the formulations in equation 4.4. In this equation F_a is a force amplitude, the subscript c indicates current and subscripts 1 and 2 indicate either the first or second wave in a flow with bichromatic waves. A flow with bichromatic waves is written as: $U_{tot} = U_c + U_{a_1} cos(\omega_1 t + \epsilon_1) + U_{a_2} cos(\omega_2 t + \epsilon_2)$ in which ϵ is the phase shift.

$$\begin{aligned} F_a(0) &= 0.5 \cdot \rho \cdot D \cdot L \cdot C_{D_c} \cdot U_c^2 + \sum_{i=1}^{2} (0.25 \cdot \rho \cdot D \cdot L \cdot C_{D_i} \cdot U_{a_i}^2) \\ F_a(f_1) &= \rho \cdot D \cdot L \cdot \sqrt{C_{D_c} \cdot C_{D_1}} \cdot U_c \cdot U_{a_1} + 0.25 \cdot \rho \cdot \pi \cdot D^2 \cdot L \cdot C_{M_1} \cdot \dot{U}_{a_1} \\ F_a(f_2) &= \rho \cdot D \cdot L \cdot \sqrt{C_{D_c} \cdot C_{D_2}} \cdot U_c \cdot U_{a_2} + 0.25 \cdot \rho \cdot \pi \cdot D^2 \cdot L \cdot C_{M_2} \cdot \dot{U}_{a_2} \\ F_a(2f_1) &= 0.25 \cdot \rho \cdot D \cdot L \cdot U_{a_1}^2 \cdot C_{D_1} \\ F_a(2f_2) &= 0.25 \cdot \rho \cdot D \cdot L \cdot U_{a_2}^2 \cdot C_{D_2} \\ F_a(f_1 + f_2) &= \rho \cdot D \cdot L \cdot \sqrt{C_{D_1} \cdot C_{D_2}} \cdot U_{a_1} \cdot U_{a_2} \\ F_a(f_1 - f_2) &= \rho \cdot D \cdot L \cdot \sqrt{C_{D_1} \cdot C_{D_2}} \cdot U_{a_1} \cdot U_{a_2} \end{aligned} \tag{4.4}$$

Using the coefficients found for the regular waves and interpolating from them and the same for the current, the force amplitudes are found. In figure 4.22 the difference between the force amplitude estimated with equations 4.4 and the measured force amplitude is shown. From this figure, it is clear that the first-order wave forces and the constant drag force are modelled quite accurately. More accurately compared to the accuracy of the classic Morison equation shown in figure 4.21. It is important to note that with the rewritten Morison

equation the second-order wave forces, as well as wave-wave interaction are still not accurately taken into account. This is caused by a single coefficient still being used both for wave-wave interaction, first-order and second-order wave forces.

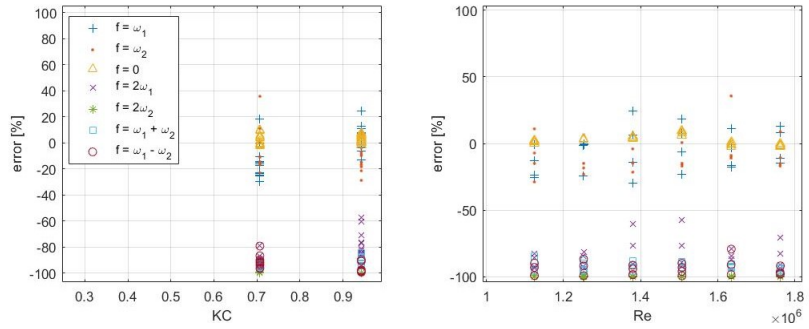

Figure 4.22: Error between the force amplitude found with equation 4.4 and the measured force amplitude for the identified force frequencies

Irregular waves

The rewritten Morison equation is found to be a viable method of finding the forces in a flow with bichromatic waves and current. The bichromatic waves were used as a simple irregular wave pattern. Now, the rewritten equation is used to find the drag forces in a wave spectrum and current.

To be able to do this, C_D and C_M are needed for every regular wave of which the irregular wave pattern consists. The experimental range in this research is too limited to be used, and the previous research could not fill the gap. Instead, the values recommended by SNAME are used: $C_D = 0.65$ and $C_M = 2$ [44]. It must be noted that these values are based on experiments which do not include free surface effects. C_D and C_M for the current are obtained from the experimental results. As only the steady and oscillatory part are separated the rewritten Morison equation effectively becomes the three-term Morison equation for irregular waves. Using these values the accuracy of the rewritten Morison equation is compared to the classical Morison equation. The rewritten Morison equation models the forces more accurately, with $R^2 = 56$ % on average, compared to the classical use of the Morison equation, with $R^2 = 47\%$. The values of R^2 are thought to be relatively low as phase differences and noise decrease the values, but also the flow description of the irregular waves is less accurate, decreasing the R^2 value.

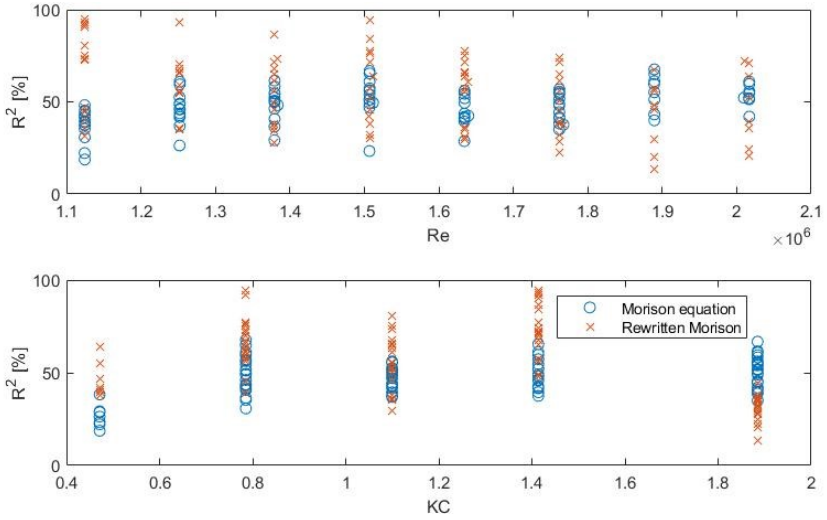

Figure 4.23: Accuracy of the classic Morison equation and the rewritten Morison equation for irregular waves, represented by R^2, shown for Re and KC. The spread shown in both is due to a variation over the range of respectively KC and Re

The results for the separate experiments are shown in figure 4.23. The figure shows that the accuracy does not strongly depend on Re, but does depend on KC. The rewritten Morison is more accurate up to a KC value of 1.5, after that the accuracy decreases. This could be due to the free surface effects and their influence on C_M (discussed in paragraph 4.2) not being taken into account in the used coefficients.

Only the current and waves are considered separately with different C_D and C_M but already show improvement. This thus gives promise that the method can improve estimates of drag forces, and should be investigated in future research.

Summary

It is concluded that using the rewritten Morison equation results in similar or better results compared to the classical method of using the Morison equation. Data from regular wave experiments can be used to find the drag forces in irregular waves and can lead to more accurate predictions of the forces. More research providing better estimates for C_D and C_M for the various waves in a wave spectrum might further improve the estimate of the drag force.

5

Conclusion

In the transition towards renewable energy, energy generating devices in the shape of vertical cylinders are placed offshore. Currents and waves induce hydrodynamic forces on these cylinders, for which the model to date remains incomplete. This research aims to find C_D and C_M and to investigate the drag of a surface piercing cylinder in flow with high Reynolds and low Keulegan-Carpenter numbers. Utilizing experiments in which the current velocity, wave and peak period, wave height and wave type were varied, the research goal was fulfilled. Simulations were conducted focussing on the free surface and end effects. This led to the following conclusions.

1) C_D and C_M are found to depend on both KC and Re for $9.7{\cdot}10^5 < \text{Re} < 2.0{\cdot}10^6$ and $0.49 < \text{KC} < 1.9$. C_D varies between 0.4 and 0.5 and C_M between 0 and 3.5. C_M goes above values of 2 due to free surface effects. The coefficients of irregular waves are found to not be equal to the coefficients of regular waves with a period equal to the peak period of the waves spectrum. For irregular waves, C_D showed little dependency on KC but did show dependency on Re. For C_M a dependency on KC was found, but not as strong as the regular wave counterpart.

2) For the researched range, evidence was found of second-order harmonic wave forces, wave-wave interaction and vortex shedding inducing periodic forces on the cylinder. Second-order wave forces were found for regular waves, wave-wave interaction for bichromatic waves. Vortex shedding was identified for all flows with Reynolds numbers above $1.2 \cdot 10^6$, becoming more significant above $1.5 \cdot 10^6$. It should be noted that this can be due to frequency lock-in. The Morison equation underestimates the second-order wave forces and the wave-wave interaction and does not include vortex shedding. This leads to inaccurate modelling of flows including current and waves.

3) The free surface effects and end effects are found to influence C_D and C_M. The free surface effects are found again to increase C_M. The influence of the free surface and end effects on C_D are opposite, as the free surface effect increases C_D and end effects decrease it. Increasing the length over diameter ratio increases drag coefficient, with the maximum increase when there is no free end. Estimations indicate that when both free surface effects and end effects are eliminated C_D will decrease. These are estimations and further research is needed.

4) It was found that the coefficients found for irregular waves were not equal to or in the same way dependent on Reynolds and Keulegan-Carpenter compared to their regular counterparts. However, a method of estimating the drag force in irregular waves with data from regular waves is investigated. By rewriting the Morison equation the separate flows of which a total flow consists, and their known coefficients, the drag forces are found to be more accurately modelled compared to the classical use of the Morison equation.

It is recommended to further investigate the modelling capabilities of the rewritten Morison equation for various wave spectra. Secondly, further research into free surface and end effects is needed to create a better understanding of the dependency of the drag on the Froude number and the length of diameter ratio of the cylinder. Thirdly, the vortex shedding frequency is thought to have locked in with the natural frequency. Additional experiments in similar ranges of Re and KC and different natural frequencies are needed to find the true force amplitude caused by vortex shedding. Lastly, it is advised to conduct more experiments for the range of Re and KC in which energy generating devices are placed, as there is still a gap in research.

A

Designing of and discussion on experiments

The experiments were designed to adhere to the description given in paragraph 1.3.2. The design process consisted of choosing a facility and designing a test setup within the limits of the facility. The experiments and the expected inaccuracies are discussed afterwards.

A.1. Methodology choice

In the field of hydrodynamics, there are three main methods of modelling a problem: experimentally, analytically, or using simulations. Experiments have problems but are proven to be successful at obtaining the required results, as can be seen in the research of Boccotti et al. [9] and Sarpkaya [67]. Due to the high ranges of Reynolds in which the problem exists combined with waves and free surface effects, analytical methods such as using potential theory or the linearized Navier-Stokes equation are not viable options [75]. As discussed in paragraph 1.1.5, simulations are not yet capable of accurately simulation the whole problem.

As experiments can give the most accurate results, these are chosen as the main method.

A.2. Facility choice

The available test facilities have been evaluated. To obtain the required results, the test facility will have to be able to generate waves, simulate current, allow for free surface effects, and have the correct dimensions to allow for high Reynolds numbers and the required waves. Three test facilities with these specifications available at the department Maritime and Transport Technology at the Technical University of Delft were looked into: the flume tank, towing tank no. 1, and towing tank no. 2 [81]. Their specifications are shown in table A.1. For the flume tank, no data of the waves that can be generated is available as the wavemaker would have to be built.

Table A.1: Limitations of the different test facilities for respectively the maximum velocity, wavelength, water depth and tank width

	$U_{max}[m/s]$	λ [m]	max depth [m]	B [m]
Flume tank	0.9	-	0.3	2
Towing tank no. 1	7	0.3 - 6	2.5	4.22
Towing tank no. 2	3	0.4 - 6.5	1.25	2.75

The specifications of the tanks dictate the maximum and minimum values of Re and KC at which can be tested. Not only the wavelength that can be generated but also the water depth limits the wavelength as unwanted shallow water effects can occur. The width of the tank should be 2.4 times the diameter of the cylinder according to ITTC [41], as wall effects will influence the results if there is not enough distance between the cylinder and walls. The maximum speed limits the current velocity that can be simulated and dictates thus the maximum Reynolds number. The other limitations are due to maximum forces allowed on the carriage of the towing tanks. Conservative estimates are made for the designing of the experiments.

Taking these limits into account, the test facilities have been evaluated. The resulting values for which can be tested in each tank are shown in table A.2. From this table, it can be concluded that towing tank no.1 is preferred as it is the only one that allows tests within the range of interest. The limitations of this tank are shown in appendix A.3.

Table A.2: The possible ranges for each test facility for a certain diameter of cylinder

	D [m]	L [m]	Re	KC	Relative depth
Flume tank	0.003	0.03	240 - 2200	0.86 - 1.9	0.05 - 0.05
Towing tank no. 1	0.4	0.5	$2.8 \cdot 10^5$ - $1.5 \cdot 10^6$	0.25 - 2.8	1.6 - 0.42
Towing tank no. 2	0.2	0.25	$8.1 \cdot 10^4$ - $3.2 \cdot 10^5$	0.28 - 2	0.80 - 0.19

A.3. Limitations of the test facility

The experiments are conducted using towing tank no. 1. This towing tank is 142 meters long, 4.22 meters wide, and 2 - 2.5 meters deep. It is equipped with a wavemaker which can generate waves between 1.5 and 6 meters long [81]. From ing. C. P. Poot additional information was obtained. The weight of the carriage of towing tank no. 1 is 6000 kg, the maximum force in x-direction is 6 kN, the maximum arm from the suspension to the wheels is 8 meters, the maximum upwards force per wheel is 15.4 kN, and the minimum wave period that can be generated is 1 second. Through ComFLOW simulations (described in paragraph 3), it was found that the minimum length of the cylinder above water should be 0.7 m. The sampling frequency used at towing tank no. 1 is 100 Hz for the displacements. The waves and forces are sampled at 1000 Hz, but before saving they are filtered with a second-order analogue filter at 100 Hz, damping all frequencies above 100 Hz. These limits all influence the allowable test range.

A.3.1. Calculations for the designing of experiments

Using the values obtained, a design and test ranges which fall within the limits are calculated. In these calculations, the diameter of the cylinder, underwater length of the cylinder, and maximum current velocity were chosen such that boundary conditions are satisfied. As there are various assumptions within the calculations, they are shown in detail. The results are shown in table A.3.

Keulegan-Carpenter and Reynolds number

The Keulegan-Carpenter number has been calculated using equation A.1. In this equation $U_{m_{max}}$ is the maximum velocity amplitude of the wave (0.39 m/s), T is the maximum wave period (2 s), and D is the cylinder diameter (0.4 m).

$$KC = \frac{U_{m_{max}} \cdot T}{D} = 1.9 \tag{A.1}$$

The velocity amplitude does not include the current velocity and is calculated using deep water wave theory, in which the path of a particle is assumed to be a circle. The wave period is calculated in the same way. The relative water depth will be at least 0.42, which is just intermediate. It is thus assumed that the deepwater assumption will not lead to large errors. This is further discussed in the last paragraph of this chapter.

The Reynolds number is calculated using equation A.2. In the equation U_{max} is the maximum current velocity (4.7 m/s) and ν the dynamic viscosity. The dynamic viscosity of freshwater at a temperature of 12° C. This gives a value of $\nu = 1.24 \cdot 10^{-6}$ [1].

$$Re = \frac{U_{max} \cdot D}{\nu} = 1.52 \cdot 10^6 \tag{A.2}$$

Force per wheel

One of the limits is the maximum force on the wheels. To check if this limit is not exceeded, the gravitational force and the forces on the test specimen are considered. For calculating the gravitational forces, it is assumed that the test set-up is weightless, as its weight will be small compared to the weight of the carriage. Equation A.3 shows the calculation. Here m is the mass of the carriage (6000 kg), g is the gravitational acceleration (9.81 m/s^2), and n_w is the number of wheels (4).

$$F_g = \frac{m \cdot g}{n_w} = 14.7 \text{ kN} \tag{A.3}$$

The forces on the test specimen in flow are difficult to predict, as a correct C_D and C_M are needed. As discussed in chapter 1, this is not available. To ensure that the maximum forces are not exceeded, the conservative estimates of C_D = 1.2 and C_M = 2.0 were used [44]. Using the Morison equation A.4, the maximum force ($F_{M_{max}}$) is estimated. In this equation L is the underwater length of the cylinder (0.5 m), ρ the water density (997 kg/m^3), $\dot{U}_{m_{max}}$ the maximum flow acceleration (6 m/s^2).

$$F_{M_{max}} = L \cdot (0.5 \cdot C_D \cdot \rho \cdot (U_{max} + U_{m_{max}})^2 \cdot D + 0.25 \cdot C_M \cdot \rho \cdot \dot{U}_{m_{max}} \cdot D^2) = 2.87 \text{ kN} \tag{A.4}$$

This force is not applied at the wheel. By finding the moment due to the force and then dividing it by the arm to the wheel, the force at the wheel is found. It is assumed that the clamping point of the cylinder in the suspension will be 0.75 meter above still water level and that the force is evenly distributed over the underwater area of the cylinder. Using equation A.5, the force per wheel is found. The found value is exactly within limits. In this equation l is the distance from the suspension to the wheel (8 m).

$$F_w = F_g + \frac{F_{M_{max}}(0.5 \cdot L + 0.75)}{0.5 \cdot n_w \cdot l} = 15.3 \text{ kN} \tag{A.5}$$

Test time

The test time is of importance to the quality of the tests as more data will minimize errors. To find the test time, the maximum acceleration is found, using equation A.6. In this equation c_f is the estimated friction coefficient (0.1).

$$a_a = \frac{(m \cdot g \cdot c_f) - F_M}{m} = 0.5 \ m/s^2 \tag{A.6}$$

The deceleration is calculated as well as breaking will take time at high speeds. It is calculated using equation A.7

$$a_d = \frac{(m \cdot g \cdot c_f)}{m} = 1.0 \ m/s^2 \tag{A.7}$$

The minimum test time is calculated in equation A.8. In this equation L_{tank} is the driving length of the tank (116 m), $t_{test_{min}}$ is the minimum test time, and t_{stab} is the estimated stabilizing time of the flow (2 s).

$$t_{test_{min}} = \frac{L_{tank}}{U_{max}} - \frac{U_{max}}{a_a} - \frac{U_{max}}{a_d} - t_{stab} = 8.8 \text{ s} \tag{A.8}$$

Conclusion

All the boundary conditions are met. The resulting maximum test values according to the initial, conservative calculations are shown in table A.3.

Table A.3: Maximum test values according to conservative design calculations.

KC	**Re**	**D [m]**	**L [m]**	$t_{test_{min}}$ **[s]**	F_w **[kN]**
0 - 2	$9.71 \cdot 10^5$ - $1.52 \cdot 10^6$	0.4	0.5	8.8	15.3

A.4. Final design

The detailed design was made by ing. C. P. Poot and ing. J. G. den Ouden. It is shown in detail in figure A.1 The overall setup is discussed in paragraph 2.1.

To house this relatively large setup, a superstructure was built on the towing tank. This was made up of 0.15x0.15 m steel H-beams, shown in light green in figure 2.1, and 0.08x0.08 m aluminium beams, shown as light grey. This created a stiff structure in which the setup was placed. The setup itself was placed in the superstructure using linear slide bearings and rotation bearings. This connection allowed the cylinder to move freely in the direction of the flow, and around the axis perpendicular to the flow and length of the cylinder. These movements were prohibited by steel rods of the length of 1 m at the top of the cylinder, and 0.85 m at the top of the setup. The rods were divided into two and H3-C3-200kg-3B loadcells by Zemic were placed in between. This allows for the forces in the direction of current to be measured.

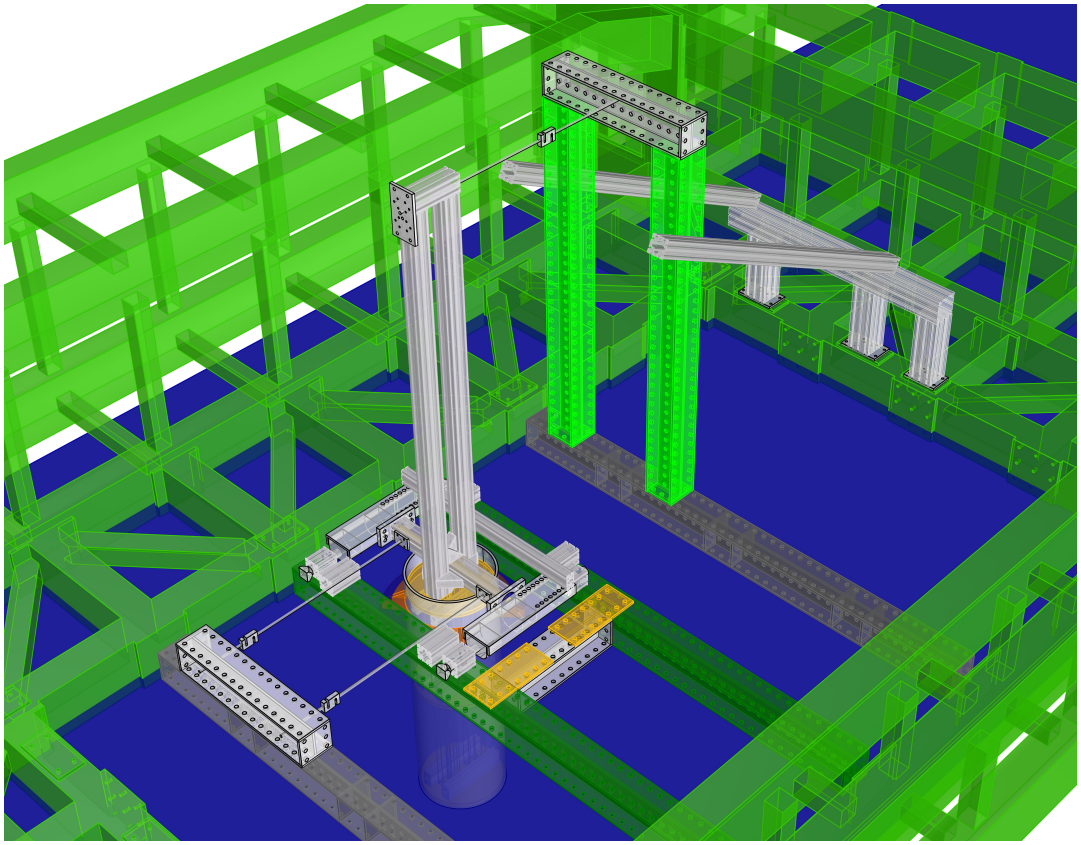

Figure A.1: Perspective view of the test setup

A.5. Discussion of experiments

As experiments are conducted in the physical world, imperfections and effects which are not of interest affect the results. These are discussed in this paragraph.

Measurements

The first inaccuracies to discuss are within the measurements of the setup. Using multiple measuring tools and measurements, it was attempted to minimize the error. However, the measurements were found to vary, thus leaving room for inaccuracies. This means that the water depth, all distances and underwater length of the cylinder can have a centimetre variance. For the measurements of the forces and the wave amplitudes, respectively loadcells and wave probes were used. The loadcells have found to have a maximum measuring error of 0.8% in the range of 0 to 200 kg. The wave probes have a maximum measuring error of 2.44% in a range of 0 to 0.2 m. These inaccuracies were used in paragraph 2.4.

Time variance
The experiments were conducted over four weeks. During this time, the water temperature varies, water evaporates, and changes in the setup can occur. This was anticipated, and thus every other day the water temperature and water level were checked and if deemed necessary, water was added. It was found that the water temperature varied between 17.8 and 17.3°C. The water depth is estimated to have varied half a centimetre over the course of the experiments.

Before every run, a zero run was conducted to check variance over time. Over the course of the experiments, tests were repeated. It was concluded that the changes that occurred during the four weeks did not influence the results of the experiments.

Test setup
The imperfections in the test setup could also have influenced the results.

Firstly, the cylinder was designed to be stiffly mounted in the setup. However, to be able to measure the forces, loadcells were used. These act as stiff springs, and thus allow some movements, influencing the results.

The cylinder used in the experiments has been through multiple processes to create a smooth surface. This was deemed to be successfully done, except for 2 imperfections found on the surface. On the outflow side of the cylinder, at about 400 mm below the waterline seven indents in a horizontal row, each indent about 5 mm long, 2 mm high and 0.5 mm deep. On the port side of the cylinder, at about 350 mm below the waterline, another indent of approximately 5 mm long, 2 mm high and 0.5 mm deep was identified. Other than these imperfections, the cylinder was found to be completely smooth. Measurements of the cylinder were taken to determine if it was round and straight. The results are shown in figure A.2. It is found that the diameter of the cylinder varies 0.3%.

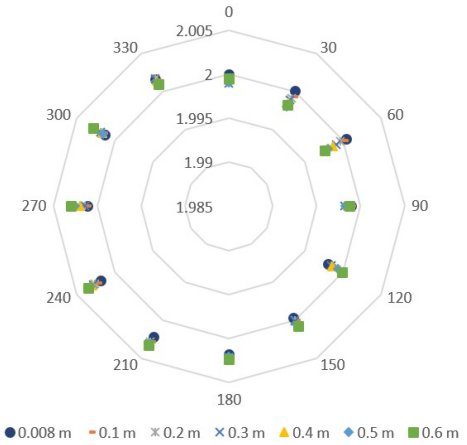

Figure A.2: Measurements of the cylinder. On the radial axis are degrees, on the tangential axis the measured radius in metres with a total range of 0.02 m. The legend shows the measurement on different distances from the bottom of the cylinder

To protect the equipment during testing, spray protection was placed on the cylinder, 0.54 m above the waterline. This spray protection did deflect water during the experiments, especially at higher velocities. To evaluate the influence, tests were done with and without the spray protection, and the force and arm to the force were compared. It was theorized that if the spray protection induced forces, this would influence the arm to the application point of the forces due to its location. It was concluded that the spray protection did not influence the results.

A.5.1. Non-linearity waves
It was attempted to generate the linear waves described in paragraph 2.2. However, as the experiments were conducted in a physical test facility, errors are introduced. Before the tests were conducted the wavemaker and the waves have been calibrated. Two wave probes were used, placed 3.72 m apart before the cylinder was placed.

The waves were made using the flap-type wavemaker and they were found to have a slightly non-linear quality, as the wave peaks were slightly higher and the wave troughs were slightly flattened when compared to a sinusoidal wave. As shown in table A.4, this non-linearity is largest for the waves with a shorter wave

period. This is thought to be the result the flap-type wavemaker creating waves in the whole water column, thus creating waves low in the water column, which is unrealistic for linear waves with a shorter wave period. The data seems to support this, as shown in table A.4.

Table A.4: Error between the measured and model waves for each wave period and the wave spectra

T_p [s]	1.00	1.24	1.48	1.72	1.96
1. $(\eta_{meas} - \eta_{lin})/\eta_{lin}$	11%	8.4%	4.7%	3.7%	1.6%
2. $(\eta_{max} - \eta_{meas})/\eta_{meas}$	5.9%	0.026%	7.0%	3.6%	5.6%
3. $(H_{m0} - H_s)/H_s$	-1.4%	-15%	-20%	-21%	-30%

The table also shows the error between the mean wave height and the maximum wave height. This difference is caused by both the wave flap-type deviating between waves, as well as the water in the towing tank being disturbed by previous tests. In the table η_{meas} is the measured average wave height, η_{lin} is the linear wave amplitude, η_{max} is the maximum measured wave height, H_{m0} the spectral significant wave height and H_s the significant wave height.

To find the accuracy of the modelling of the JONSWAP spectrum, long runs of 1200 seconds were tested. From this, the H_{m0} was found and compared to the H_s that was attempted to be modelled. There are various problems with the reliability of the found results. Firstly, H_{m0} is compared to H_s. These are not the same values, as H_{m0} is generally slightly larger. The second cause of inaccuracy is due to the length of the tests, as reflections of the waves in the towing tank are added to the spectrum. The reflections can also influence the spectrum since waves can start breaking, leading to dissipation of energy. Lastly, it was found that for the spectra with longer wave periods, the wave probe was not large enough to measure all wave heights, thus the large wave heights were not accurately measured, leading to a decrease in the estimated H_{m0}. All in all, the errors shown in table A.4 are large, but this does not necessarily mean that there are problems with the modelling of the spectra but are more likely a result of problematic estimation of H_{m0}.

Second-order Stokes theory

In literature, it is found that the waves used are expected to have a non-linear quality due to the wave steepness. It is found that the waves are best modelled using the second-order Stokes theory [38].

This theory uses the linear wave theory and adds a second-order Stokes correction. This second-order Stokes correction has a frequency twice that of the linear wave, but a phase speed equal to the linear wave, binding them. The Stokes second-order theory models waves with a higher peak and flatter troughs compared to linear wave theory, which is also what was found to be the case in paragraph A.5 for the regular waves in the experiments.

Stokes second-order theory was implemented in the calculations of the research and compared to the results obtained using linear wave theory. It was found that the second-order Stokes correction has an amplitude of 7% of the amplitude of the linear wave. The overall modelling accuracy of the Morison equation is checked with also new coefficients found using the second-order Stokes theory in the least squares methods. With the second-order Stokes theory an increased from R^2 = 72% to R^2 = 73% for regular waves and from R^2 = 48% to R^2 = 53% for irregular waves. The bichromatic waves used a steepness of 0.02 and thus fall in the range where the linear wave theory is the best model for the waves. The modelling accuracy is found to only increase slightly, which is expected as it is found that the inaccuracy of the Morison equation comes from phase shifts, noise in the measurements, and the Morison equation not taking vortex shedding into account and underestimating second-order wave forces and wave-wave interaction.

An important note should be made, however. Using linear wave theory it is found that the Morison equation underestimates second-order wave forces. However, the second-order wave forces have the same frequency as the second-order Stokes correction. It is possible that the second-order wave forces found are partially caused by the non-linearity of the used waves. Using the nonlinear wave theory increased the estimated second-order wave force. But, as the second-order wave forces were previously underestimated with almost 100%, as shown in figure 4.22, an almost unchanged discrepancy is still found between the modelled force using the Morison equation and the measured force.

Bibliography

[1] Engineering Toolbox, 2004. URL https://www.engineeringtoolbox.com/water-dynamic-kinematic-viscosity-d{_}596.html.

[2] M. F. Ahmad, M. R. M. Haniffah, A. Kueh, and E. H. Kasiman. Numerical study on drag and lift coefficients of a marine riser at high Reynolds number using COMSOL multiphysics. In *IOP Conference Series: Earth and Environmental Science*, volume 476. Institute of Physics Publishing, jun 2020. doi: 10.1088/1755-1315/476/1/012075.

[3] A. Ajdin. New model trials of offshore floating solar underway - Offshore Energy, 2020. URL https://www.offshore-energy.biz/new-model-trials-of-offshore-floating-solar-underway/.

[4] S. D. Apte. Fourier Series Representation of Periodic Signals. In *Signals and Systems: Principles and Applications*, chapter 3, pages 236–241. Cambridge University Press, 2016.

[5] F. Aristodemo, G. Tripepi, D. Algieri Ferraro, and P. Veltri. An experimental and numerical study on solitary wave loads at cylinders near the bed. *Ocean Engineering*, 195(November 2019):106747, 2020. ISSN 00298018. doi: 10.1016/j.oceaneng.2019.106747. URL https://doi.org/10.1016/j.oceaneng.2019.106747.

[6] P. W. Bearman. Understanding and predicting vortex-induced vibrations. *Journal of Fluid Mechanics*, 634:1–4, 2009. ISSN 00221120. doi: 10.1017/S0022112009990851.

[7] P. W. Bearman, J. R. Chaplin, J. G. Graham, J. K. Kostense, and G. Klopman. The loading on a cylinder in post-critical flow beneath periodic and random waves. 1985.

[8] M. M. Bernitsas. Harvesting energy by flow included motions. In *Springer Handbook of Ocean Engineering*, pages 1163–1244. Springer International Publishing, jan 2016. ISBN 9783319166490. doi: 10.1007/978-3-319-16649-0_47.

[9] P. Boccotti, F. Arena, V. Fiamma, and A. Romolo. Two small-scale field experiments on the effectiveness of Morison's equation. *Ocean Engineering*, 57:141–149, jan 2013. ISSN 00298018. doi: 10.1016/j.oceaneng.2012.08.011.

[10] A. D. Boon. Drag of a surface piercing cylinder in fast current and low waves, 2020.

[11] B. Bosma. On the Design, Modeling, and Testing of Ocean Wave Energy Converters. page 87, 2013. URL http://ir.library.oregonstate.edu/xmlui/handle/1957/41003.

[12] C. E. Brennen. A Review of Added Mass and Fluid Inertial Forces, 1982.

[13] L. M. Bricheno, J. Wolf, and J. Aldridge. Distribution of natural disturbance due to wave and tidal bed currents around the UK. *Continental Shelf Research*, 109:67–77, oct 2015. ISSN 18736955. doi: 10.1016/j.csr.2015.09.013.

[14] B. W. Byrne and G. T. Houlsby. Foundations for offshore wind turbines, dec 2003. ISSN 1364503X.

[15] G. Capannelli and O. T. Gudmestad. Hydrodynamic Coefficients for Calculation of Hydrodynamic Loads on Offshore Truss Structures Hydrodynamic Coefficients for Calculation of Hydrodynamic Loads on Offshore Truss Structures. 8339(October 2017), 1996. doi: 10.1016/0951-8339(95)00023-2.

[16] S. Chakrabarti. Handbook of Offshore Engineering, Volumes 1-2, 2005. URL https://app.knovel.com/web/toc.v/cid:kpHOEV0001/viewerType:toc//root{_}slug:handbook-of-offshore?kpromoter=marc.

[17] J. R. Chaplin and P. Teigen. Steady flow past a vertical surface-piercing circular cylinder. *Journal of Fluids and Structures*, 18:271–285, 2003. doi: 10.1016/j.jfluidstructs.2003.07.009. URL www.elsevier.nl/locate/jnlabr/yjfls.

[18] P. C. Chu, Yi. Qi, Y. Chen, P. Shi, and Q. Mao. South China Sea Wind-Wave Characteristics. Part I: Validation of Wavewatch-III Using TOPEX/Poseidon Data. *Journal of Atmospheric and Oceanic Technology*, 21(11):1718–1733, nov 2004. ISSN 0739-0572. doi: 10.1175/JTECH1661.1. URL http://journals.ametsoc.org/doi/10.1175/JTECH1661.1.

[19] L. J. Clancy. *Aerodynamics*. Wiley, 1975. ISBN 0470158379.

[20] A. M. Cobbin, P. K. Stansby, and P. W. Duck. The hydrodynamic damping force on a cylinder in oscillatory, very-high-Reynolds-number flows. *Applied Ocean Research*, 17(5):291–300, oct 1995. ISSN 01411187. doi: 10.1016/0141-1187(96)84791-2.

[21] G. R. Cook and E. Simiu. Hydrodynamic forces on vertical cylinders and the lighthill correction. *Ocean Engineering*, 1989. doi: 0029-8018/89.

[22] R. G. Dean, R. A. Dalrymple, and R. T. Hudspeth. Force Coefficients From Wave Project I and II Data Including Free Surface Effects. *Society of Petroleum Engineers of AIME*, 1981. doi: 10.2118/9103-PA.

[23] DNV GL. DNVGL-ST-0437, 2016. URL http://www.dnvgl.com.

[24] M. A. Donelan, F. Anctil, and J. C. Doering. A simple method for calculating the velocity field beneath irregular waves. Technical report, 1992.

[25] T. Ducrocq, L. Cassan, J. Chorda, and H. Roux. Flow and drag force around a free surface piercing cylinder for environmental applications. *Environmental Fluid Mechanics*, 17(4), 2017. ISSN 1567-7419. doi: 10.1007/s10652-016-9505-9.

[26] A. B. Z. Feys. Support structure for offshore solar: The proposal of a new concept. Technical report, Delft University of Technology, 2020.

[27] FLOW-3D. VOF - What's in a Name? Volume of Fluid Method. URL https://www.flow3d.com/resources/cfd-101/modeling-techniques/vof-whats-in-a-name/.

[28] Fluid Mechanics 101. [CFD] What is the difference between Upwind, Linear Upwind and Central Differencing?, 2018. URL https://www.youtube.com/watch?v=JVE0fNkc540{&}t=1140s.

[29] H. Fukuoka, S. Hirabayashi, and H. Suzuki. The effects of free surface and end cell on flow around a finite circular cylinder with low aspect ratio. *Marine Science and Technology*, 21:145–153, 2016. doi: 10.1007/s00773-015-0338-x.

[30] A. Ghadirian and H. Bredmose. Detailed force modelling of the secondary load cycle. *Journal of Fluid Mechanics*, 889:A211–A2130, 2020. ISSN 14697645. doi: 10.1017/jfm.2020.70.

[31] J. Grue, G. Bjorshol, and O. Strand. Higher harmonic wave exciting forces on a vertical cylinder. *Applied Mathematics*, 2, 1993.

[32] O. T. Gudmestad and J. J. Connor. Linearization methods and the influence of current on the nonlinear hydrodynamic drag force. *Applied Ocean Research*, 5(4):184–194, oct 1983. ISSN 01411187. doi: 10.1016/0141-1187(83)90032-9.

[33] Q. Guo and Z. Xu. Simulation of Deep-Water Waves Based on JONSWAP Spectrum and Realization by MATLAB. *9th International Conference on Geoinformatics*, 22:1–4, 2011. doi: 10.1109/GeoInformatics.2011.5981100.

[34] F. H. Harlow and J. E. Welch. Numerical calculation of time-dependent viscous incompressible flow of fluid with free surface. *Physics of Fluids*, 8(12):2182–2189, 1965. ISSN 10706631. doi: 10.1063/1.1761178.

[35] K. Hasselmann, T. P. Barnett, E. Bouws, H. Carlson, and Et al. Measurements of Wind-Wave Growth and Swell Decay during the Joint North Sea Wave Project (JONSWAP). *Coastal Engineering*, 7(1):399–404, 1973. ISSN 03783839. doi: 10.1016/j.coastaleng.2015.09.010.

[36] J. Helder and P. van der Plas. ComFLOW User Group, 2019.

[37] C. W. Hirt and B. D. Nichols. Volume of fluid (VOF) method for the dynamics of free boundaries. *Journal of Computational Physics*, 39(1):201–225, 1981. ISSN 10902716. doi: 10.1016/0021-9991(81)90145-5.

[38] L. H. Holthuijsen. *Waves in Oceanic and Coastal Waters*. Cambridge University Press, Cambridge, sep 2010. ISBN 978-0-521-86028-4. URL https://app.knovel.com/web/toc.v/cid:kpWOCW0002/viewerType:toc//root{_}slug:waves-in-oceanic-coastal/url{_}slug:nonlinear-permanent-waves?issue{_}id=kt007N2OF1{&}hierarchy=kt007N2OF1.

[39] M. Isaacson, J. Baldwin, and C. Niwinski. Estimation of drag and inertia coefficients from random wave data. *Journal of Offshore Mechanics and Arctic Engineering*, 113(2):128–136, 1991. ISSN 1528896X. doi: 10.1115/1.2919908.

[40] ITTC. The Specialist Committee on Waves. In *Final Report and Recommendations to the 23rd ITTC*, volume 2, pages 505–551, 723–736, 2002. URL https://ittc.info/media/1469/waves.pdf.

[41] ITTC. ITTC – Recommended Procedures and Guidelines - Captive Model Test Procedures. 7.5-02-06-02 (Revision 04). page 20, 2014.

[42] Y. Iwagaki and T. Asano. Hydrodynamic Forces on a Circular Cylinder due to Combined Wave and Current Loading. In *Proceedings of the Coastal Engineering Conference*, volume 3, pages 2857–2874. ASCE, jan 1985. ISBN 0872624382. doi: 10.9753/icce.v19.191.

[43] H. Jasak. *Error analysis and estimation for finite volume method with applications to fluid flow*. PhD thesis, University of London, 1996.

[44] J. M. J. Journée and W. W. Massie. *Offshore Hydromechanics*. Delft, 1 edition, 2001.

[45] P. Justesen. Hydrodynamic Forces on Large Cylinders in Oscillatory Flow. *Ocean Engineering*, 115(4):497–514, 1989.

[46] C. Kalogeri, G. Galanis, C. Spyrou, D. Diamantis, F. Baladima, M. Koukoula, and G. Kallos. Assessing the European offshore wind and wave energy resource for combined exploitation. *Renewable Energy*, 101:244–264, feb 2017. ISSN 18790682. doi: 10.1016/j.renene.2016.08.010.

[47] G. H. Keulegan and L. H. Carpenter. Forces on Cylinders and Plates in an Oscillating Fluid. *Journal of Research of the National Bureau of Standards*, 60(5), 1958.

[48] E. Konstantinidis and D. Bouris. Drag and inertia coefficients for a circular cylinder in steady plus low-amplitude oscillatory flows. *Applied Ocean Research*, 65:219–228, apr 2017. ISSN 01411187. doi: 10.1016/j.apor.2017.04.010.

[49] B. Koo, J. Yang, S. M. Yeon, and F. Stern. Reynolds and froude number effect on the flow past an interface-piercing circular cylinder. *International Journal of Naval Architecture and Ocean Engineering*, 6(3):529–561, sep 2014. ISSN 20926790. doi: 10.2478/IJNAOE-2013-0197.

[50] A. Kozakiewicz, B. M. Sumer, and J. Fredsøe. Cross-flow vibrations of cylinder in irregular oscillatory flow. *Journal of Waterway, Port, Coastal and Ocean Engineering*, 120(6):515–534, nov 1994. ISSN 0733950X. doi: 10.1061/(ASCE)0733-950X(1994)120:6(515).

[51] M. Latheef, N. Abdulla, and M. F. M. Jupri. Wave current interaction: Effect on force prediction for fixed offshore structures. In *MATEC Web of Conferences*, volume 203. EDP Sciences, sep 2018. doi: 10.1051/matecconf/201820301011.

[52] T. M. Lewis, A. Von Jouanne, and T. K.A. Brekken. Modeling and control of a slack-moored two-body wave energy converter with finite element analysis. In *2012 IEEE Energy Conversion Congress and Exposition, ECCE 2012*, pages 938–945, 2012. ISBN 9781467308014. doi: 10.1109/ECCE.2012.6342718.

[53] Y. Liu, S. Li, Q. Yi, and D. Chen. Wind profiles and wave spectra for potential wind farms in South China Sea. Part II: Wave spectrum model. *Energies*, 10(1), 2017. ISSN 19961073. doi: 10.3390/en10010127.

[54] B. Lund, B. K. Haus, J. Horstmann, H. C. Graber, R. Carrasco, N. J.M. Laxague, G. Novelli, C. M. Guigand, and T. M. Özgökmen. Near-surface current mapping by shipboard marine X-band radar: A validation. *Journal of Atmospheric and Oceanic Technology*, 35(5):1077–1090, may 2018. ISSN 15200426. doi: 10.1175/JTECH-D-17-0154.1.

[55] K. Merz. A Review of the Morison Equation for Calculating Hydrodynamic Loads on Vertically-Oriented Cylinders, 2010.

[56] G. Moe and O. T. Gudmestad. Predictions of Morison-Type Forces in Irregular Waves at High Reynolds Number. *International Journal of Offshore and Polar Engineering*, 8(4), 1998.

[57] J. R. Morison, J. W. Johnson, and S. A. Schaaf. The Force Exerted by Surface Waves on Piles. *Journal of Petroleum Technology*, 2(05):149–154, may 1950. ISSN 0149-2136. doi: 10.2118/950149-g.

[58] P. Naaijen, K. Trulsen, and E. Blondel-Couprie. Limits to the extent of the spatio-temporal domain for deterministic wave prediction. *International Shipbuilding Progress*, 61(3-4):203–223, 2014. ISSN 15662829. doi: 10.3233/ISP-140113.

[59] V. Negro, J. López-Gutiérrez, M. Dolores Esteban, P. Alberdi, M. Imaz, and J. Serraclara. Monopiles in offshore wind: Preliminary estimate of main dimensions. Technical report, 2017. URL `www.offshorewind.biz/2016/03/14/first-veja-`.

[60] E. D. Obasaju, P. W. Bearman, and J. M.R. Graham. A study of forces, circulation and vortex patterns around a circular cylinder in oscillating flow. *Journal of Fluid Mechanics*, 196:467–494, 1988. ISSN 14697645. doi: 10.1017/S0022112088002782.

[61] Orcina Ltd. OrcaFlex, 1987. URL `https://www.orcina.com/webhelp/OrcaFlex/Content/html/Waves,Wavespectra.htm`.

[62] A. Osinowo, X. Lin, D. Zhao, and Z. Wang. Long-term variability of extreme significant wave height in the South China Sea. *Advances in Meteorology*, 2016, 2016. ISSN 16879317. doi: 10.1155/2016/2419353.

[63] W. Qiu, D.Y. Lee, H. Lie, J. M. Rousset, T. Mikami, S. Sphaier, L. Tao, X. Wang, and V. Magarovskii. Numerical benchmark studies on drag and lift coefficients of a marine riser at high Reynolds numbers. *Applied Ocean Research*, 69:245–251, dec 2017. ISSN 01411187. doi: 10.1016/j.apor.2017.10.010. URL `https://pureportal.strath.ac.uk/en/publications/numerical-benchmark-studies-on-drag-and-lift-coefficients-of-a-ma`.

[64] K. Raed and C. Guedes Soares. Variability effect of the drag and inertia coefficients on the Morison wave force acting on a fixed vertical cylinder in irregular waves. *Ocean Engineering*, 159:66–75, jul 2018. ISSN 00298018. doi: 10.1016/j.oceaneng.2018.03.066.

[65] B. H. Riise, J. Grue, A. Jensen, and T. B. Johannessen. High frequency resonant response of a monopile in irregular deep water waves. *Fluid Mechanics*, 853:564–586, 2018. doi: 10.1017/jfm.2018.499. URL `https://doi.org/10.1017/jfm.2018.499`.

[66] D. Rockwell, M. Ozgoren, and N. Saelim. Self-excited oscillations of vertical and horizontal cylinders in presence of a free-surface. *Fluid Mechanics and its Applications*, 75:201–210, 2004. ISSN 09265112. doi: 10.1007/978-94-007-0995-9_14.

[67] T. Sarpkaya. In - Line And Transverse Forces, On Cylinders In Oscillatory Flow At High Reynolds Numbers. In *Offshore Technology Conference*. Offshore Technology Conference, apr 1976. doi: 10.4043/2533-MS. URL `http://www.onepetro.org/doi/10.4043/2533-MS`.

[68] T. Sarpkaya. Force on a circular cylinder in viscous oscillatory flow at low keulegan—carpenter numbers. *Journal of Fluid Mechanics*, 165:61–71, 1986. ISSN 14697645. doi: 10.1017/S0022112086002999.

[69] T. Sarpkaya. Hydrodynamic Damping and Quasi-Coherent Structures at Large Stokes Numbers. *Journal of Fluids and Structures*, pages 909–928, 2001. doi: 10.1006/j.

[70] T. Sarpkaya. On the parameter β = Re/KC = D^2/νT. *Journal of Fluids and Structures*, 21(4):435–440, dec 2005. ISSN 08899746. doi: 10.1016/j.jfluidstructs.2005.08.007.

[71] T. Sarpkaya and M. Storm. In-line force on a cylinder translating in oscillatory flow. *Applied Ocean Research*, 7(4):188–196, oct 1985. ISSN 01411187. doi: 10.1016/0141-1187(85)90025-2.

[72] N. J. Shankar, H. Cheong, and K. Subbiah. Forces on a Smooth Submarine Pipeline in Random Waves-A Comparative Study. Technical report, Amsterdam, 1987.

[73] A. A. R. Sreenivasan and B. K. Iyer. Enhanced wall turbulence model for flow over cylinder at high Reynolds number. *AIP Advances*, 9(9), sep 2019. ISSN 21583226. doi: 10.1063/1.5118421.

[74] P. K. Stansby, G. N. Bullock, and I. Short. Quasi-2-D Forces on a Vertical Cylinder in Waves. *Journal of Waterway, Port, Coastal, and Ocean Engineering*, 109(1):128–132, feb 1983. ISSN 0733-950X. doi: 10.1061/(ASCE)0733-950X(1983)109:1(128).

[75] V. L. Streeter and E. B. Wylie. Fluid mechanics (seventh ed.). 1979.

[76] B. M. Sumer and J. Fredsoe. *Hydrodynamics around cylindrical structures*, volume 26. 1997. ISBN 9812700390.

[77] B. M. Sumer and J. Fredsøe. Flow around a cylinder in steady current. pages 1–35. World Scientific, mar 2010. ISBN 978-981-270-039-1. doi: 10.1142/9789812795748_0001.

[78] T. Teich, N. Groll, and R. Weisse. Long-term statistics of potentially hazardous sea states in the North Sea 1958–2014. *Ocean Dynamics*, 68(11):1559–1570, nov 2018. ISSN 16167228. doi: 10.1007/s10236-018-1210-4.

[79] K. M. Theresa Kleefsman and A. E. P. Veldman. An improved volume-of-fluid method for wave impact. *ECCOMAS 2004 - European Congress on Computational Methods in Applied Sciences and Engineering*, (August), 2004.

[80] M. J. Thorsen and S. Sævik. Simulating riser VIV in current and waves using an empirical time domain model. *Proceedings of the International Conference on Offshore Mechanics and Arctic Engineering - OMAE*, 2, sep 2017. doi: 10.1115/OMAE2017-61217.

[81] TU Delft. Facilities, 2020. URL `https://www.tudelft.nl/3me/over/afdelingen/maritime-and-transport-technology/research/ship-hydromechanics/facilities/`.

[82] M. Van Der Eijk and P. R. Wellens. A compressible two-phase flow model for pressure oscillations in air entrapments following green water impact events on ships. *International Shipbuilding Progress*, 66(4):315–343, 2020. ISSN 15662829. doi: 10.3233/ISP-200278.

[83] P. van der Plas. 1. Introduction — ComFLOW 4.2.0-alpha documentation. URL `http://poseidon.housing.rug.nl/sphinx/intro.html`.

[84] A. E. P. Veldman. *Computational Fluid Dynamics*. Groningen, 2012.

[85] V. Venugopal, K. S. Varyani, and P. C. Westlake. Drag and inertia coefficients for horizontally submerged rectangular cylinders in waves and currents. *Proceedings of the Institution of Mechanical Engineers Part M: Journal of Engineering for the Maritime Environment*, 223(1):121–136, 2009. ISSN 14750902. doi: 10.1243/14750902JEME124.

[86] R. L. P. Verley and G. Moe. The forces on a cylinder oscillating in a current. Technical report, The Norwegian Institute of Technology, 1979.

[87] J. Wang, S. Fu, R. Baarholm, J. Wu, and C. M. Larsen. Fatigue damage of a steel catenary riser from vortex-induced vibration caused by vessel motions. *Marine Structures*, 39:131–156, dec 2014. ISSN 09518339. doi: 10.1016/j.marstruc.2014.07.002.

[88] P. R. Wellens and M. Borsboom. A generating and absorbing boundary condition for dispersive waves in detailed simulations of free-surface flow interaction with marine structures. *Computers and Fluids*, 200:104387, mar 2020. ISSN 00457930. doi: 10.1016/j.compfluid.2019.104387.

[89] C. H.K. Williamson. In-line response of a cylinder in oscillatory flow. *Applied Ocean Research*, 7(2):97–106, apr 1985. ISSN 01411187. doi: 10.1016/0141-1187(85)90040-9.

[90] C. H.K. Williamson and A. Roshko. Vortex formation in the wake of an oscillating cylinder, jul 1988. ISSN 10958622.

[91] G. Xiang and C. Guedes Soares. Improved dynamical modelling of freely falling underwater cylinder based on CFD. *Ocean Engineering*, 211, sep 2020. ISSN 00298018. doi: 10.1016/j.oceaneng.2020.107538.

[92] Z. Yuan and Z. Huang. Morison coefficients for a circular cylinder oscillating with dual frequency in still water: an analysis using independent-flow form of Morison's equation. *Journal of Ocean Engineering and Marine Energy*, 1(4):435–444, nov 2015. ISSN 21986452. doi: 10.1007/s40722-015-0030-6.

[93] M. M. Zdravkovich and P. W. Bearman. Flow Around Circular Cylinders—Volume 1: Fundamentals. *Journal of Fluids Engineering*, 120(1):216–216, mar 1998. ISSN 0098-2202. doi: 10.1115/1.2819655.